IEEE Access
Multidisciplinary ⋮ Rapid Review ⋮ Open Access Journal

Received 22 February 2026, accepted 20 March 2026, date of publication 26 March 2026, date of current version 31 March 2026.

Digital Object Identifier 10.1109/ACCESS.2026.3678088

RESEARCH ARTICLE

FEM-Based Quantification of Eddy-Current Losses for MV Cables in Trefoil Formation With Non-Magnetic Screens

MARKO ŠUĆUROVIĆ[1], DARDAN KLIMENTA[2], NIKOLAY HINOV[3,4], (Senior Member, IEEE), DRAGAN TASIĆ[5], (Senior Member, IEEE), MLADEN BANJANIN[6], AND DARIUS ANDRIUKAITIS[7], (Member, IEEE)

[1]Faculty of Technical Sciences, University of Kragujevac, 32102 Čačak, Serbia
[2]Faculty of Technical Sciences, University of Priština in Kosovska Mitrovica, RS 38220 Kosovska Mitrovica, Serbia
[3]CoE "National Center of Mechatronics and Clean Technologies", 1000 Sofia, Bulgaria
[4]Faculty of Computer Systems and Technologies, Technical University in Sofia, 1000 Sofia, Bulgaria
[5]Faculty of Electronic Engineering, University of Niš, 18104 Niš, Serbia
[6]Faculty of Electrical Engineering, University of East Sarajevo, 71123 East Sarajevo, Bosnia and Herzegovina
[7]Faculty of Electrical and Electronics Engineering, Kaunas University of Technology, 44249 Kaunas, Lithuania

Corresponding author: Nikolay Hinov (hinov@tu-sofia.bg)

This work was supported by the Operational Program "Research, Innovation and Digitalisation for Smart Transformation 2021–2027" through the "National Center of Excellence For Mechatronics and Clean Technologies" under Project BG16RFPR002-1.014-0006-C01.

ABSTRACT Circulating- and eddy-current losses occur in non-magnetic screens and armors of three medium-voltage (MV) single-core cables installed in trefoil formation, where they are bonded and earthed at both ends. According to IEC 60287-1-1, eddy-current losses in non-magnetic screens and armors should be neglected, whereas the technical brochure CIGRÉ TB 880 recommends that these losses should always be taken into account. For the considered screen bonding design, a reliable quantitative separation of circulating- and eddy-current losses is therefore essential. Such a separation cannot be performed accurately while simultaneously using experimental methods alone, but it can be achieved through a combination of analytical modeling and finite element method (FEM)-based electro–magneto–thermal simulations. This paper proposes and applies a new hybrid FEM-based procedure for the quantitative determination of circulating- and eddy-current losses in MV cables. The method is applied to Cu/XLPE/CTS/PVC/AWA/PVC 1/C 19/33 kV (BS 6622) cables with twelve different conductor cross-sections. The accuracy of the proposed procedure is verified by comparisons with IEC-based analytical calculations that account for eddy-current losses in accordance with the technical brochures CIGRÉ TB 272 and CIGRÉ TB 880. The FEM-based electro–magneto–thermal models are calibrated and validated using experimental data already published for PL 1 × 300 RM 6/10 kV cables. The developed calibration strategy represents another novelty. The results demonstrated that, for the BS 6622 cables with conductor cross-sections ranging from 70 to 1000 mm^2, the screen and armor eddy-current loss factors lie within the ranges 0.00094–0.03625 and 0.00719–0.1951, respectively. The deviations between the FEM- and IEC-based eddy-current loss factors range from −6.398% to 5.302%, demonstrating a very good agreement.

INDEX TERMS Circulating-current loss factor, eddy-current loss factor, finite element method (FEM), screen bonding design, single-core power cable, trefoil formation.

I. INTRODUCTION

There are several analytical models for calculating eddy-current loss factors for the case of three single-core cables in trefoil formation with non-magnetic screens and armors bonded and earthed at both ends. However, the

The associate editor coordinating the review of this manuscript and approving it for publication was Yun Seng Lim.

available models can generally be categorized as follows: (i) precise or approximate, but computationally complicated [1], [2]; (ii) simple but relatively imprecise, yet standardized by the International Electrotechnical Commission (IEC) [3], [4]; and (iii) precise and simple, but not included in the relevant IEC standard [5], [6]. For a design without armors and with screens bonded and earthed at both ends, the common practice for including eddy-current losses in analytical procedures is as follows. Firstly, the circulating-current loss factor is calculated for the design where screens are bonded and earthed at both ends. Secondly, the eddy-current loss factor is calculated for the design where screens are bonded and earthed at one end. Finally, these two loss factors are summed to obtain the total loss factor used in ampacity calculations [3], [6].

However, according to [7], separate calculation of circulating- and eddy-current losses in order to obtain total losses may lead to a large error, reaching almost twice the actual loss value. Moreover, another principle is reported in the literature [8], [9]: eddy-current losses can be obtained as the difference between measured total screen losses and calculated (or measured) circulating-current losses, after which the corresponding loss factors can be determined. Furthermore, for the considered design, the IEC-based ampacity calculation procedure ignores the thermal effect of eddy-current losses [3]; nevertheless, this does not constitute a deviation from the above-mentioned principles. In addition, experimental procedures used for determining the total loss factor rely on the second principle [1], [8], [9], [10].

A similar principle should also be applied in finite element method (FEM)-based procedures [11], [12], [13], but no such procedure has been developed yet. FEM-based procedures are needed owing to the fact that current distributions in the conductors and screens of power cables are non-uniform in most practical cases [8]. Another important reason is that FEM-based modeling is generally more accurate than purely experimental or analytical approaches, as well as their combinations. The absence of a FEM-based procedure that can quantitatively separate eddy-current losses from the circulating ones therefore motivates the present research.

According to the historical perspective presented in [14], the basic analytical models to calculate the circulating- and eddy-current losses in metallic screens of power cables were established during the late 1920s and early 1930s. That historical survey reviewed publications dealing with experimental or analytical determination of circulating- and/or eddy-current loss factors from the 1920s until late 1996. According to [13], in that period only Labridis and Dokopoulos [12] addressed FEM-based determination of loss factors. In addition, the review paper [15] incorporated the historical perspective from [14] and analyzed the literature on magnetic field effects and loss factor calculations until 2021. From that review, only [16] can be singled out as a reference where FEM was applied to determine losses due to circulating and eddy currents in non-magnetic screens. In contrast, a significant number of FEM-based studies published until 2021 considered the same problem primarily for cables with magnetic screens [17], [18], [19]. A review of relevant research papers published from 2021 onwards is provided in the following two paragraphs.

A 3D FEM-based procedure for in-depth analysis of electromagnetic interactions in actual three-core armored power cables – considering aspects that are neglected under IEC assumptions – was utilized in [20]. The procedure was tested on more than 700 cable arrangements, showing differences below 5% for conductor and screen losses and below 20% for armor losses, when compared with corresponding IEC-based and experimental results [20]. A hybrid procedure combining FEM and IEC standard formulas for power cables with Milliken conductors was proposed in [21], with deviation in conductor losses of less than 1% relative to IEC-based calculations [21]. In addition, losses in copper conductors and aluminum armor of a three-core power cable were determined analytically in [22], and the obtained results were compared with those generated by FEM- and IEC-based procedures.

A simple and effective 2D FEM-based model for analyzing low-frequency magnetic fields generated by single-core power cables with copper screens bonded and earthed at both ends (in both trefoil and flat formations) was proposed in [23]. In addition to magnetic flux density profiles computed at various heights above the Earth surface, the influence of copper screens on magnetic field reduction was also analyzed in [23]. FEM-based simulations and experimental investigations of the thermal behavior of power cables in unfilled ducts were conducted in [24]. The FEM-based simulations provided conductor and screen temperatures that agree well with the corresponding experimental data and can be further used to determine associated losses [24]. A similar FEM-based thermal analysis of single-core power cables with aluminum screens bonded and earthed at both ends was presented in [25], which was also supported by appropriate experimental data. Based on the literature review, for the considered screen bonding design it is evident that a hybrid FEM-based procedure enabling quantitative separation of eddy-current losses from the circulating ones has not been established. This paper addresses the identified research gap.

In particular, this paper proposes a hybrid FEM-based procedure that combines: (i) an IEC-based analytical modeling approach, accounting for eddy-current losses in accordance with CIGRÉ TB 272 and CIGRÉ TB 880, and (ii) FEM-based electro–magneto–thermal modeling. The same IEC-based analytical modeling is also used as a reference procedure to verify the accuracy of the proposed one. Circulating- and eddy-current losses in metallic screens and armors are calculated for twelve different medium-voltage (MV) cables of the type Cu/XLPE/CTS/PVC/AWA/PVC 1/C 19/33 kV (BS 6622), with compacted stranded copper conductors the cross-sections of which range from 70 mm^2 to 1000 mm^2, using both the reference analytical procedure and the proposed hybrid FEM-based procedure. It is assumed that three MV single-core cables of the given type are laid directly in the soil in trefoil touching formation, with copper screens and aluminum armors bonded and earthed at both ends. The analytical and FEM-based models used, as well as all assumptions introduced, follow relevant IEC standards [3], [26], [27], [28], CIGRÉ technical brochures [5], [6], BS standards [29], and research papers that discuss the application of those IEC and BS standards [4], [30]. For the considered screen bonding design, eddy-current losses are separated quantitatively from circulating-current losses.

The proposed hybrid FEM-based procedure is calibrated and validated using existing experimental data for three PL 1 × 300 RM 6/10 kV cables in trefoil non-touching formation, with stranded copper conductors of 300 mm^2, mass-impregnated (MI) paper insulation, and lead sheaths. The experimental data are taken from [9], while all FEM-based electro–magneto–thermal simulations are performed in COMSOL [31]. The calibration is carried out in seven steps. Furthermore, the difference between measured and calculated total sheath losses is found to be 2.688%, and, in general, small deviations are obtained with respect to the experimental data reported in [9].

Following the abstract and introduction, this paper presents the computational domains, material properties, and service conditions (Section II), mathematical modeling (Section III), calibration of FEM-based models (Section IV), results and discussion (Section V), and conclusions (Section VI). A list of references is provided at the end of the paper.

II. COMPUTATIONAL DOMAINS, MATERIAL PROPERTIES AND SERVICE CONDITIONS

This paper considers the following 40 m × 40 m computational domains:

- A domain with a 10 kV underground line consisting of three PL 1 × 300 RM 6/10 kV cables in trefoil non-touching formation that corresponds to an experimental circuit used in [9] and Figure 1a – First Computational Domain.
- A domain with a 33 kV underground line consisting of three Cu/XLPE/CTS/PVC/AWA/PVC 1×300 RMC/25 19/33 kV cables, installed in trefoil non-touching formation according to Figure 1a – Second Computational Domain.
- A domain with a 33 kV underground line consisting of three Cu/XLPE/CTS/PVC/AWA/PVC 1×300 RMC/25 19/33 kV cables in trefoil touching formation that corresponds to a computational domain used in [4] and Figure 2a – Third Computational Domain.
- 11 additional domains each containing a 33 kV underground line with three cables of the type Cu/XLPE/CTS/PVC/AWA/PVC 1/C 19/33 kV in trefoil touching formation according to Figure 2a and conductors of rated cross-section different from 300 mm^2.

Construction elements of the PL 1 × 300 RM 6/10 kV cable are shown in Figure 1b, while construction elements of the Cu/XLPE/CTS/PVC/AWA/PVC 1 × 300 RMC/25 19/33 kV cable are shown in Figure 2b. Figures 1a and 2a show First and Third Computational Domains, respectively. Second Computational Domain can be obtained by replacing the PL 1 × 300 RM 6/10 kV cables with the Cu/XLPE/CTS/PVC/AWA/PVC 1 × 300 RMC/25 19/33 kV cables in Figure 1a, while each of the 11 additional computational domains can be obtained by replacing the BS

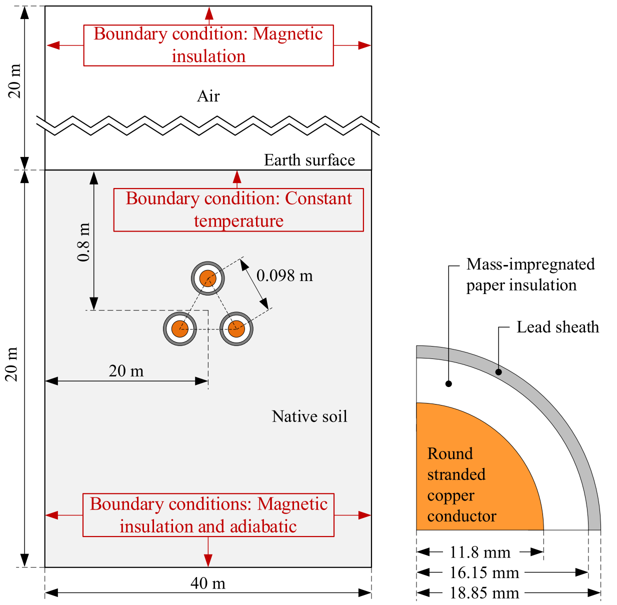

(a) Computational domain (b) Cable construction elements

FIGURE 1. First computational domain with a 10 kV underground line consisting of three PL 1 × 300 RM 6/10 kV cables in trefoil non-touching formation and construction elements of the PL 1 × 300 RM 6/10 kV cable. First computational domain corresponds to an experimental circuit used in [9].

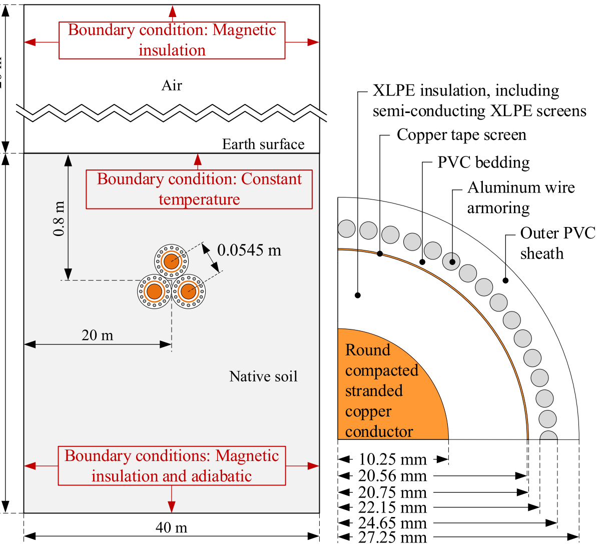

(a) Computational domain (b) Cable construction elements

FIGURE 2. Third computational domain with a 33 kV underground line consisting of three Cu/XLPE/CTS/PVC/AWA/PVC 1 × 300 RMC/25 19/33 kV cables in trefoil touching formation and construction elements of the Cu/XLPE/CTS/PVC/AWA/PVC 1 × 300 RMC/25 19/33 kV cable. Third computational domain corresponds to a series of computational domains used in [4].

6622 cables with cables of the same type and different cross-section in Figure 2a. Accordingly, the second and additional computational domains are not illustrated separately. The first three computational domains will be used for the calibration of FEM-based models. For the experimental circuit used in [9], the installation depth of the PL 1 × 300 RM 6/10 kV cables is not provided, therefore it is assumed that the installation depth to the center of the trefoil non-touching formation L corresponds to that considered in [4], i.e., it is $L = 0.8$m.

The external dimensions and boundary conditions for these computational domains were chosen based on [3], [4], [28], [30], and [31]. In addition, some dimensions of the PL 1×300 RM 6/10 kV cable were not given within the description of the experiments in [9] and they were estimated based on the data found in [32] and [33]. According to IEC 60228 [34], the maximum diameter of a round stranded copper conductor with a rated cross-section of 300 mm^2 should be 23.1 mm. This is 0.5 mm less than the corresponding diameter in Figure 1b. However, the maximum diameter from Figure 1b can be considered possible because the technology of cable conductor manufacturing in the 1920s and 1930s was at a lower degree of precision than it is today.

For the purposes of thermal finite element analyses in COMSOL [4], [30], and [31], any MV cable of the type Cu/XLPE/CTS/PVC/AWA/PVC 1/C 19/33 kV needs to be modeled with an equivalent cable consisting of the copper conductor, cross-linked polyethylene (XLPE) insulation, equivalent/enlarged copper screen and outer polyvinyl chloride (PVC) sheath with outer radii r_1, r_4, r_7 and r_8, respectively. For the Cu/XLPE/CTS/PVC/AWA/PVC 1×300 RMC/25 19/33 kV cable in Figure 2b, these outer radii are as follows: $r_1 = 10.25$ mm, $r_4 = 20.56$ mm, $r_7 = 24.65$ mm and $r_8 = 27.25$ mm. The equivalent cable construction is created based on IEC 60287-1-1 [3]. In particular, the semi-conducting XLPE screens of the conductor and insulation are added to XLPE insulation, while the copper tape screen, PVC bedding and aluminum wire armor are represented with an equivalent/enlarged copper screen. Since the PVC bedding is added to the equivalent/enlarged copper screen, it means that the thermal resistance of the PVC bedding should be added to the thermal resistance of the outer PVC sheath. Furthermore, the outer radii r_2, r_3, r_5, and r_6 correspond to the conductor screen, actual insulation layer, insulation screen and PVC bedding, respectively. The procedure is described in [4].

Table 1 outlines the thermal, electrical, dielectric and magnetic properties of non-magnetic metals, insulation materials, native soil and air used in IEC- and FEM-based models. These material properties are taken from the IEC 60287 standards [3], [26], [27], professional literature [35], [36], and several research papers [4], [30], [37]. The parameters appearing in Table 1 are as follows: k_t is the thermal conductivity in W/(K·m); ρ_e is the electrical resistivity at 20 °C in nΩ·m; α_{20} is the temperature coefficient of electrical resistivity at 20 °C in 1/K; ε_r is the relative electric permittivity; $\tan\delta$ is the loss factor for the insulation materials at a system frequency $f = 50$ Hz; and μ_r is the relative magnetic permeability. It is assumed that the relative electric permittivity ε_r of non-magnetic metals is approximately 1, that the relative magnetic permeability μ_r of all non-magnetic materials is approximately 1, and that the native soil in the computational domains (in Figures 1a and 2a, etc.) was first dried-out and then normally moist, or only normally moist.

TABLE 1. Thermal, electrical, dielectric and magnetic properties of materials used for IEC- and FEM-based modeling.

Material	k_t W/(K·m)	ρ_e nΩ·m	α_{20} 1/K	ε_r –	$\tan\delta$ –	μ_r –
Al at 20 °C	239	28.4	0.00403	1	–	1
Cu at 20 °C	385	17.241	0.00393	1	–	1
Pb at 20 °C	34.5	214	0.004	1	–	1
XLPE	0.286	10^{24}	–	2.5	0.004	1
PVC	0.167	10^{22}	–	8	–	1
MI paper	0.167	10^{22}	–	4	0.01	1
Native soil	0.833	10^{11}	–	3	–	1
Air	–	10^{23}	–	1	–	1

Ampacity calculations are performed for PL 1 × 300 RM 6/10 kV cables and for Cu/XLPE/CTS/PVC/AWA/PVC 1/C 19/33 kV cables with conductor cross-sections ranging from 70 to 1000 mm^2, in order to quantify eddy-current losses in non-magnetic screens and armors of MV cables installed in trefoil non-touching and trefoil touching formations. Service conditions and constructional data for the MV cables of the given types are taken from [4] and [9]. According to [4] and [9], the following service conditions are analyzed: cables installed directly in the soil, in trefoil non-touching or touching formation, with non-magnetic metallic screens and armors bonded and earthed at both ends or at one end; referent soil or ambient temperature $\theta_{rs} = 20$°C or $\theta_{rs} = 15$°C; thermal conductivity of the native soil $k_{t,s} = 0.4$ W/(K·m) for the dried-out state and $k_{t,s} = 0.833$ W/(K·m) for the normally moist state; and the current $I = 100$ A or the ampacity I_{cp} in A. The service conditions such as installation of the PL 1×300 RM 6/10 kV cables in trefoil non-touching formation, $\theta_{rs} = 20$°C and $I = 100$ A correspond to the experiments conducted in [9], while the remaining service conditions are taken from the manufacturer's technical documentation and they correspond to the IEC- and FEM-based simulations with the BS 6622 cables performed in [4], or are assumed for the purposes of the calibration of FEM-based models.

III. MATHEMATICAL MODELING

A. IEC-BASED ANALYTICAL MODELING CONSIDERING EDDY-CURRENT LOSESS

In this particular case, the cable ampacity (in A) should be calculated based on IEC 60287-1-1 [3], IEC 60287-2-1 [26], CIGRÉ TB 272 [5], and CIGRÉ TB 880 [6] using the following formula:

$$I_{cp} = \left\{ \frac{\theta_{C,cp} - \theta_{rs} - W_{d,l}[0.5T_1 + n(T_2 + T_3 + T_4)]}{R_C[T_1 + n(1 + \lambda_1)T_2 + n(1 + \lambda_1 + \lambda_2)(T_3 + T_4)]} \right\}^{0.5} \tag{1}$$

where $\theta_{C,cp}$ is the continuously permissible temperature of a cable in °C ($\theta_{C,cp} = 70$°C for 10 kV MI paper-insulated cables and $\theta_{C,cp} = 90$°C for XLPE-insulated cables); $W_{d,l}$ stands for the dielectric losses per phase and unit length of one cable in W/m; T_1 is the total thermal resistance of the semi-conducting and insulation layers between a conductor and its accompanying metallic screen in K·m/W; n is the number of conductors in a cable; T_2 is the thermal resistance of the PVC bedding in K·m/W – for a BS 6622 cable only; T_3 is the thermal resistance of the outer PVC sheath in K·m/W – for a BS 6622 cable only; and T_4 is the thermal resistance of the surroundings in K·m/W. Other parameters used in this formula are: R_C maximum AC resistance of a conductor per unit length at $\theta_{C,cp} = 70$ °C or $\theta_{C,cp} = 90$°C in Ω/m (that takes into account the skin and proximity effects), and λ_1 and λ_2 are the screen and armor loss factors, respectively (in particular, λ_1 or λ_2 is the ratio of the total losses due to circulating and eddy currents in one non-magnetic screen/sheath $W_{1,l}$, in W/m, or armor $W_{2,l}$, in W/m, to the losses in one conductor $W_{C,l}$, in W/m, respectively). The values of the maximum AC resistance R_C for the cables used are taken from the manufacturer's technical documentation, or estimated based on those data according to IEC 60228 [34].

According to CIGRÉ TB 880 [6], the screen loss factor λ_1 can be defined by

$$\lambda_1 = \lambda_1' + F_s\lambda_1'' \tag{2}$$

where λ_1' is the screen circulating-current loss factor, λ_1'' is the screen eddy-current loss factor, and F_s is a correction coefficient for the screen eddy-current loss factor. The screen circulating-current loss factor λ_1' is equal to zero for metallic screens and armors bonded and earthed at one end [3].

According to IEC 60287-1-1 [3], CIGRÉ TB 272 [5] and CIGRÉ TB 880 [6], the armor loss factor λ_2 is

$$\lambda_2 = \lambda_2' + F_{ar}\lambda_2'' \tag{3}$$

where λ_2' is the armor circulating-current loss factor, λ_2'' is the armor eddy-current loss factor, and F_{ar} is a correction coefficient for the armor eddy-current loss factor. Although the aluminum armors of Cu/XLPE/CTS/PVC/AWA/PVC 1/C 19/33 kV cables are made of wires, it is assumed that there are losses due to eddy currents in such wires. This assumption is based on the recommendation given in CIGRÉ TB 272 [5].

In addition, the screen circulating-current loss factor λ_1' and the armor circulating-current loss factor λ_2' are defined by [6]:

$$\lambda_1' = \lambda_{1,eq}' \frac{R_{ar}(\theta_{ar})}{R_s(\theta_s) + R_{ar}(\theta_{ar})} \tag{4}$$

and

$$\lambda_2' = \lambda_{1,eq}' \frac{R_s(\theta_s)}{R_s(\theta_s) + R_{ar}(\theta_{ar})}, \tag{5}$$

respectively. The meanings of the parameters appearing in Equations (4) and (5) are as follows [3]:

$$\lambda_{1,eq}' = \frac{R_{s,eq}}{R_C(\theta_{C,cp})} \cdot \frac{1}{1 + \left(\frac{R_{s,eq}}{X}\right)^2} \tag{6}$$

– the enlarged screen circulating-current loss factor;

$$R_{s,eq} = \frac{R_s(\theta_s)R_{ar}(\theta_{ar})}{R_s(\theta_s) + R_{ar}(\theta_{ar})} \tag{7}$$

– the equivalent AC resistance of the metallic screen and armor in parallel in Ω/m; $R_s(\theta_s)$ is the AC resistance of the metallic screen per unit length of a cable at its maximum operating temperature θ_s in Ω/m; $R_{ar}(\theta_{ar})$ is the AC resistance of the armor per unit length of a cable at its maximum operating temperature θ_{ar} in Ω/m; and X is the reactance of the equivalent/enlarged screen per unit length of a cable in Ω/m. The reactance of the equivalent/enlarged screen is calculated using the root mean square value of the mean diameters of the metallic screen and armor [3], [4]. Since the temperatures of the metallic screen and armor are functions of the current, their values are obtained by an iterative method in accordance with IEC 60287-1-1 [3]. In addition to this, the screen eddy-current loss factor λ_1'' is calculated in the same manner as in [3] and [4].

Furthermore, the correction coefficient for the screen eddy-current loss factor F_s is calculated by [3] and [6]:

$$F_s = \frac{4M^2N^2 + (M + N)^2}{4(M^2 + 1)(N^2 + 1)} \tag{8}$$

where

$$M = N = \frac{R_s(\theta_s)}{X} \tag{9}$$

are appropriate coefficients for trefoil non-touching or touching formation.

It is assumed that the procedure for calculating the armor eddy-current loss factor λ_2'' is the same as the one for calculating the screen eddy-current loss factor λ_1''. In this case, the aluminum wire armor is modeled by a cylindrical layer having the same mean radius and the same effective cross-section. Accordingly, the value of the correction coefficient F_{ar} is obtained using Equations (8) and (9) when $R_s(\theta_s)$ is replaced by $R_{ar}(\theta_{ar})$.

Thermal resistance of the surrounding soil T_4in K·m/W is calculated by [26] and [35]

$$T_4 = \frac{1}{2\pi k_{t,s}} \ln\left[\left(\frac{L}{r_8} + \sqrt{\frac{L^2}{r_8^2} - 1}\right)\frac{d_{SR}'}{d_{SR}}\frac{d_{ST}'}{d_{ST}}\right] \tag{10}$$

– for trefoil non-touching formation, or,

$$T_4 = \frac{1}{2\pi k_{t,s}} \ln\left(\frac{2L}{r_8} + \frac{L}{r_8}\right) \tag{11}$$

– for trefoil touching formation. In Equation (10), the subscripts R, S and T denote the phase cables R, S and T in trefoil non-touching formation, respectively; where the R-phase cable is the top cable in this formation. Further, in the same equation, d_{SR} is the axial spacing between the S and R phase cables in m, d_{ST} is the axial spacing between the S and T phase cables in m, d'_{SR} is the axial spacing between the S phase cable and the mirror image of the R phase cable (with respect to the earth surface) in m, and d'_{ST} is the axial spacing between the S phase cable and the mirror image of the T phase cable in m.

All remaining parameters ($W_{d,l}$, R_C, T_1, T_2 and T_3) necessary for calculating the cable ampacity using Equation (1) are determined in accordance with the standards IEC 60287-1-1 [3] and IEC 60287-2-1 [26], as well as Reference [4]. Although according to [3], dielectric losses should not be taken into account for values of the phase-to-phase voltages lower than or equal to 110 kV, the effect of these losses is considered here to reduce potential error sources.

B. FEM-BASED ELECTRO-MAGNETO-THERMAL MODELING CONSIDERING EDDY-CURRENT LOSESS

In this paper, the MV cables of the types PL 1 × 300 RM 6/10 kV and Cu/XLPE/CTS/PVC/AWA/PVC 1/C 19/33 kV installed directly in the soils according to Figures 1a and 2a, respectively, were chosen as the case studies. The dimensions from Figures 1 and 2 and the material properties from Table 1 were used as the input data to create two-dimensional coupled electro-magneto-thermal models of the considered underground cable lines.

In general, the spatiotemporal distribution of the electromagnetic and temperature fields over the computational domain in Figure 1a or 2a for the case when the MV cables are energized can be described by the system of Maxwell's and heat conduction equations in the following way [31], [38]:

$$\nabla \times \vec{H} = \vec{J}_C + \frac{\partial \vec{D}}{\partial t} \tag{12}$$

$$\nabla \times \vec{E} = -\frac{\partial \vec{B}}{\partial t} \tag{13}$$

$$\nabla \cdot \vec{B} = 0 \tag{14}$$

$$\nabla \cdot \vec{D} = \rho_q \tag{15}$$

$$\nabla \cdot (k_t \nabla \theta) + Q_v = \rho c_p \frac{\partial \theta}{\partial t} \tag{16}$$

where $\vec{H}$ is the magnetic field strength vector in A/m; $\vec{J}_C$ is the conduction current density vector in A/m^2; $\vec{D}$ is the electric displacement vector in C/m^2; t is the time in s; $\vec{E}$ is the electric field strength vector in V/m; $\vec{B}$ is the magnetic induction vector in T; ρ_q is the volume charge density in C/m^3; k_t is the thermal conductivity in W/(K·m); θ is the temperature in K; Q_v is the volume power of heat sources in W/m^3; ρ is the density in kg/m^3; and c_p is the specific heat at constant pressure in J/(kg·K). Specifically, the conduction current density vector $\vec{J}_C$ represents the sum of the source current density vector due to the differences in electric potential $\vec{J}_S$ and the induced current density vector due to time-varying magnetic fields $\vec{J}_E$, while the partial derivative $\partial\vec{D}/\partial t$ represents the displacement current density vector due to time-varying electric field.

To simplify the analysis of the coupled electro-magneto-thermal field, the FEM-based modeling is based on the following assumptions: (i) Except for the copper conductors, copper screens, lead sheaths and aluminum armors, which are nonlinear, isotropic and homogeneous, other blocks or subdomains are linear, isotropic and homogeneous. (ii) Electrical resistivity of the copper conductors, copper screens, lead sheaths and aluminum armors is dependent on the temperature, i.e., it is nonlinear. (iii) The temporal dependence of electromagnetic field is time-harmonic, and heat transfer processes are independent of time (in a steady-state). (iv) The coupling between electromagnetic phenomena and heat transfer processes is bidirectional. In this regard, for any constant phase current or ampacity, an increase in the thermal conductivity of the surrounding soils leads to a decrease in temperatures of the metallic construction elements of MV cables, which also reduces their AC resistances and accompanying losses. (v) In the soils surrounding underground power cables, moisture migrates under the influence of Earth's gravitational force, temperature gradient, capillary suction, vapor diffusion and certain other ambient conditions [39], [40], [41], [42]. Consequently, the thermal conductivity of the native soil changes along the directions of the spatial coordinates due to the different moisture contents. This dependence was not taken into account for the reason that the FEM-based ampacity calculation must correspond to the analytical ampacity calculation based on IEC 60287-1-1 [3] and must ensure safety of the FEM-based ampacities from an engineering point of view.

Based on the previous assumptions, a quasi-steady-state approximation of the Maxwell's equations (12)-(15) and the introduction of a vector magnetic potential $\vec{A}$ (in T·m) as

$$\vec{B} = \nabla \times \vec{A}, \tag{17}$$

it can be assumed that the time-harmonic currents flowing through the copper conductors induce circulating and/or eddy currents in the lead sheaths, copper tape screens and aluminum wire armors [43].

In the considered cases, heat sources are resistive losses in the conductors, screens, sheaths and armors due to the flows of phase, circulating and eddy currents, as well as dielectric losses in the insulation layers due to the square of the phase-to-ground voltage. The dielectric losses were calculated in accordance with [4] and used as input data for the finite element analysis in COMSOL. Specifically, in these FEM-based models, the blocks (i.e., subdomains) representing lead sheaths, copper tape screens and aluminum wire armors are defined as "coils", that is, as closed external electrical circuits or conductive paths (the External I vs. U feature within the Electrical Circuit Interface of COMSOL). These closed external electrical circuits for the case of an underground line with the Cu/XLPE/CTS/PVC/AWA/PVC 1/C 19/33 kV cables in trefoil touching formation are shown in Figure 3. Each copper tape screen and each aluminum wire armor has its own closed external electrical circuit containing one variable resistor. All these circuits are bonded together and earthed at one end directly and at the other one through separate variable resistors. The resistance of any variable resistor can be changed from zero to a certain maximum value ($>10^9\,\Omega$) to simulate an interruption in the screen or armor circuit, that is, an interruption of the conductive path for circulating currents in it.

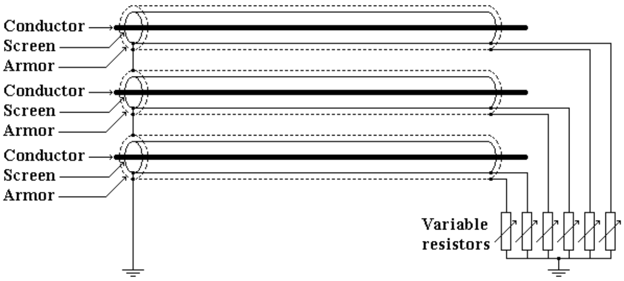

FIGURE 3. Closed external electrical circuits of the copper tape screens and the aluminum wire armors used in COMSOL for the case an underground line consisting of three Cu/XLPE/CTS/PVC/AWA/PVC 1/C 19/33 kV cables.

The volume powers of heat sources in the metallic construction elements of MV cables can be found by calculating the transferred energy of the electromagnetic field [43]:

$$Q_v = \nabla \cdot [\vec{E} \cdot \vec{H}] \tag{18}$$

When the Maxwell's equations (12)-(15) are supplemented with the following relationships [32], [43]:

$$\vec{D} = \varepsilon \vec{E} = \varepsilon_r \varepsilon_0 \vec{E} \tag{19}$$

$$\vec{B} = \mu \vec{H} = \mu_r \mu_0 \vec{H} \tag{20}$$

$$\vec{J}_C = \sigma_e(\theta) \vec{E} \tag{21}$$

the numbers of unknowns and equations are equal and the system has a unique solution. In Equations (19)-(21), ε is the electric permittivity in F/m, $\varepsilon_0 = 8.854 \cdot 10^{-12}$ F/m is the electric permittivity of vacuum, μ is the magnetic permeability in H/m, $\mu_0 = 4\pi \cdot 10^{-7}$ H/m is the magnetic permeability of vacuum, $\vec{J}_C$ is the conduction current density vector in A/m^2, and $\sigma_e(\theta)$ is the electrical conductivity depending on the temperature θ in S/m.

Taking into account Equations (19)-(21), Equation (12) becomes [38]:

$$\nabla \times \left(\frac{1}{\mu}\vec{B}\right) = \sigma_e(\theta)\vec{E} + \frac{\partial(\varepsilon \vec{E})}{\partial t} \tag{22}$$

When MV cables operate at 50 Hz, the conduction current density is significantly higher than the displacement current density. In this regard, the effect of the displacement current density can be neglected owing to the fact that the rate of change of the electric field strength ($\partial \vec{E}/\partial t$) is relatively slow [38]. This means that the second term on the right side of Equation (22) can be ignored. Accordingly, in two-dimensional case studies, taking into account Equation (17) and the assumptions introduced previously, the system of governing equations (12)-(16) reduces to [43], [44], and [45]:

$$\sigma_e(\theta)\frac{\partial A}{\partial t} - \nabla \cdot \left(\frac{1}{\mu}\nabla A\right) = J_S \tag{23}$$

$$\nabla \cdot (k_t \nabla \theta) + Q_v = 0 \tag{24}$$

where A is a component of the vector magnetic potential in T·m ($\vec{A}$ is a vector quantity in three dimensions, which conveniently reduces to a scalar quantity A in two dimensions), and J_S is the source or applied current density due to the differences in electric potential in A/m^2. Equation (23) corresponds to time-harmonic electromagnetic field, while Equation (24) corresponds to steady-state heat transfer.

Since there are no magnetic materials in the considered case studies, this means that there are only resistive losses. Thus, the volume powers of heat sources in the metallic construction elements of the considered MV cables are calculated using [31], [45]:

$$Q_v = \frac{j^2}{\sigma_e(\theta)} = j^2 \rho_e(\theta) = j^2 \rho_e[1 + \alpha_{20}(\theta - 20)] \tag{25}$$

where $j = J_S$, or

$$j = J_E = -\sigma_e(\theta)\frac{\partial A}{\partial t} \tag{26}$$

is the induced current density in A/m^2, $\rho_e(\theta) = 1/\sigma_e(\theta)$ is the electrical resistivity at the temperature θ in Ω·m, and θ is the temperature of the metallic cable construction element in °C.

The boundary conditions referred to the magnetic field must ensure the quick attenuation of the magnetic potential, that is, set its tangential component to zero. Accordingly, the homogeneous Neumann or magnetic insulation boundary condition [31], [44]

$$\vec{n} \times \vec{A} = 0 \tag{27}$$

is assigned to all external edges of the computational domains in Figures 1a and 2a.

The boundary conditions needed to predict any temperature field distribution must correspond to the Neher–McGrath method, which is incorporated in IEC 60287-1-1 [3]. In this regard, the earth surface in the computational domains from Figures 1a and 2a is represented by

$$\theta = \theta_{rs} \tag{28}$$

– Dirichlet or constant temperature boundary condition. While the left-hand, bottom and right-hand edges of these computational domains are represented by

$$\vec{n} \cdot (-k_t \nabla \theta) = 0 \tag{29}$$

– homogeneous Neumann or adiabatic boundary condition [30]. In the given Dirichlet and Neumann boundary conditions (27)-(29), θ is the unknown temperature of the boundary in K, θ_{rs} is the known temperature of the earth surface in K, and $\vec{n}$ is the outwards-oriented normal vector to the Neumann boundaries.

C. HYBRID FEM-BASED PROCEDURE

This section proposes a hybrid FEM-based procedure for quantitative separation of eddy-current losses from the circulating ones for the case of three single-core cables installed directly in the soil, in trefoil non-touching or touching formation. It is assumed that copper tape screens (or lead sheaths) and aluminum wire armors of those MV cables are bonded and earthed at both ends or at one end, depending on the rated cross-section of the conductor. The proposed hybrid FEM-based procedure combines the IEC-based analytical modeling from Section III-A with the FEM-based electromagneto-thermal modeling from Section III-B and consists of the following five steps:

Step 1: IEC-based analytical calculation of the ampacity I_{cp} and the screen/sheath and armor loss factors λ_1', λ_1'', λ_2' and λ_2'' in accordance with Section III-A for the MV cable line from Figure 2a and the set of manufacturer's service conditions from Section II. In addition to the geometric details provided in Figure 2a, the manufacturer's service conditions also include: screens/sheath and armors bonded and earthed at both ends for the conductor cross-sections between 70 mm^2 and 630 mm^2, and at one end for the conductor cross-sections of 800 mm^2 and 1000 mm^2, $\theta_{rs} = 15°$ C and $k_{t,s} = 0.833$ W/(K·m).

Step 2: FEM-based calculation of the total screen/sheath and armor losses due to circulating and eddy currents $W_{1,l}$ (in W/m) and $W_{2,l}$ (in W/m), the maximum conductor temperature $\theta_{C,\max}$ (in °C), the maximum screen/sheath temperature θ_s (in °C) and the maximum armor temperature θ_{ar} (in °C) in accordance with Section III-B. The calculation should be conducted for the design where screens/sheaths and armors are bonded and earthed at both ends, the IEC-based ampacity I_{cp} that was calculated in Step 1, and the maximum AC resistance of a conductor R_C that was taken from the manufacturer's data. Since the conductors of MV cables are geometrically modeled (in FEM) as solid conductors with geometric cross-sections, a calculation error that such an approach would cause is avoided using the values for R_C provided by the cable manufacturer. This calculation step aims to ensure that the maximum conductor temperature $\theta_{C,\max}$ is equal or very close to the continuously permissible temperature $\theta_{C,cp}$.

Step 3: FEM-based calculation of the total screen/sheath and armor losses due to eddy currents $W_{1,l}'$ (in W/m) and $W_{2,l}'$ (in W/m), the maximum conductor temperature $\theta_{C,\max}'$ (in °C), the maximum screen/sheath temperature θ_s' (in °C) and the maximum armor temperature θ_{ar}' (in °C) in accordance with Section III-B. This calculation should be carried out for the design where screens/sheaths and armors are bonded and earthed at one end, the IEC-based ampacity I_{cp} that was calculated in Step 1, and the maximum AC resistance of a conductor R_C that was used in Step 2. Such an approach eliminates losses due to circulating currents in the screens/sheaths and armors and results in a maximum conductor temperature $\theta_{C,\max}'$ that is lower than the corresponding temperature $\theta_{C,\max}$ from Step 2. This further leads to decreases in the maximum screen/sheath and armor temperatures θ_s' and θ_{ar}', which also affect their AC resistances and the associated intensities of eddy currents. At the end of this step, the eddy-current losses corresponding to the maximum temperatures of conductors, screens/sheaths and armors from Step 2 (namely: $\theta_{C,\max}$, θ_s and θ_{ar}) remain unknown.

Step 4: Repeating the calculation of the parameters from Step 3 assuming that the IEC-based ampacity I_{cp} and the maximum conductor temperature $\theta_{C,\max}$ are the same as in Step 2. The necessary increases in the temperatures of the conductors, screens/sheaths and armors to values equal or very close to those in Step 2 ($\theta_{C,\max}$, θ_s and θ_{ar}) should be achieved by gradually increasing the ambient temperature θ_{rs}. In this regard, it is assumed that a change in the ambient temperature by a few degrees Celsius cannot change the conductor AC resistance R_C to any significant extent. At the end of this step, for the design where screens/sheaths and armors are bonded and earthed at both ends, the screen/sheath circulating-current losses ($W_{1,l}'$ in W/m), the screen/sheath eddy-current losses ($W_{1,l}''$ in W/m), the armor circulating-current losses ($W_{2,l}'$ in W/m) and the armor eddy-current losses ($W_{2,l}''$ in W/m) are calculated and separated quantitatively.

Step 5: Calculating the screen/sheath and armor loss factors (Λ_1', Λ_1'', Λ_2' and Λ_2'' – numerical values) based on the screen/sheath and armor losses from Step 4 ($W_{1,l}'$, $W_{1,l}''$, $W_{2,l}'$ and $W_{2,l}''$) and comparing them with the screen/sheath and armor losses from Step 1 (λ_1', λ_1'', λ_2' and λ_2'' – analytical values).

IV. CALIBRATION OF FEM-BASED MODELS

A. CALIBRATION STRATEGY

Experimental data reported in [9] are used to develop and calibrate a reference FEM-based model that illustrates the distributions of circulating and eddy currents in non-magnetic metallic screens and armors of three Cu/XLPE/CTS/PVC/AWA/PVC 1 × 300 RMC/25 19/33 kV cables installed in trefoil touching formation. The experiment described in [9] was conducted using MV cables of the type PL 1 × 300 RM 6/10 kV for the design in which the sheaths were bonded and earthed at both ends. Although both cable types have conductors with the same rated cross-section, their constructions, insulation types, and rated voltages differ.

Furthermore, the experimental conditions reported in [9] differ from the standardized service conditions adopted for the analysis of BS 6622 cables in [4]. In particular, a transition from the computational domain shown in Fig. 1a to that shown in Fig. 2a is required, and the accuracy and consistency of the reference FEM-based model must be validated under these modified conditions. Due to differences in cable design, service conditions, and the unavailability of certain experimental parameters, the calibration strategy requires a larger number of steps than is typically necessary.

Specifically, seven calibration steps are carried out, and they are summarized below as performed in this study.

Calibration Step 1:

FEM-based calculations of distributions of temperature, magnetic field strength, and conduction current density are performed over First Computational Domain shown in Fig. 1a. In addition, sheath and conductor losses ($W'_{1,l}$, $W''_{1,l}$, $W_{1,l}$ and $W_{C,l}$), sheath loss factors (Λ'_1, Λ''_1 and Λ_1), maximum conductor temperature ($\theta_{C,\max}$), and maximum sheath temperature (θ_s) are determined. The following input data are used: phase current $I = 100$ A; trefoil non-touching formation with an axial spacing of 0.098 m; rated phase-to-phase voltage of 10 kV; and ambient temperature $\theta_{rs} = 20$°C, corresponding to the experiment reported in [9]. In addition, a soil thermal conductivity 0f $k_{t,s} = 0.4$ W/(Km) and an installation depth of $L = 0.8$ m are assumed; the conductor AC resistance is $R_C = 58.531\mu\Omega$/m, estimated according to IEC 60228 [34] while accounting for the skin and proximity effects; and the volume power of heat sources in mass-impregnated paper insulation is $Q_v = 194$ W/m^3, calculated in accordance with IEC 60287-1-1 [3] and [4]. The assumption regarding the installation depth is introduced based on the fact that the experiments reported in [9] were performed very quickly to avoid any possible effect of the thermal resistance of the surrounding soil on circulating- and eddy-current losses in lead sheaths of the three PL 1 × 300 RM 6/10 kV cables. This step represents the reference point (that is, the basic model) of the calibration strategy.

Calibration Step 2:

FEM-based calculations identical to those in Calibration Step 1 are performed for the same computational domain, with the soil thermal conductivity increased to $k_{t,s} = 0.833$ W/(Km). This step quantifies the influence of the surrounding medium on losses, loss factors, and maximum temperatures of metallic cable construction elements.

Calibration Step 3:

The PL 1 × 300 RM 6/10 kV cables are replaced by Cu/XLPE/CTS/PVC/AWA/PVC 1 × 300 RMC/25 19/33 kV cables, resulting in Second Computational Domain similar to the one shown in Fig. 1a. All FEM-based calculations from Calibration Step 2 are repeated for this domain. The only modification is the use of an appropriate volume power of heat sources in XLPE insulation, equal to $Q_v = 14.1$ W/m^3, calculated for a phase-to-phase voltage of 10 kV. This step quantifies the effect of changes in cable construction on losses, loss factors, and maximum temperatures of metallic cable construction elements.

Calibration Step 4:

The rated phase-to-phase voltage is increased from 10 kV to 33 kV to account for the difference in rated voltages between the cables tested in [9] and the BS 6622 cables. This change is introduced by updating the volume power of heat sources in XLPE insulation to 153.8 W/m^3, while all other parameters and routines remain identical to those in Calibration Step 3.

Calibration Step 5:

The effect of cable spacing is examined by reducing the axial spacing between cables, thereby transitioning from trefoil non-touching to trefoil touching formation. This results in Third Computational Domain shown in Fig. 2a. All FEM-based calculations are repeated using the parameters from Calibration Step 4, except in the case of trefoil touching formation.

Calibration Step 6:

FEM-based calculations are performed for Third Computational Domain using an ampacity of $I_{cp} = 516.558$A, calculated according to IEC 60287-1-1 [3] and IEC 60287-2-1 [26] for an ambient temperature of $\theta_{rs} = 20°$ C. This step evaluates the influence of increased phase current on losses, loss factors, and maximum temperatures of metallic cable construction elements.

Calibration Step 7:

The same FEM-based calculations as in Calibration Step 6 are carried out, but with the ambient temperature θ_{rs} reduced from 20 °C to 15 °C. The corresponding IEC-based ampacity is $I_{cp} = 534.713$ A. This final step ensures full consistency with the standardized service conditions used in [4] and completes the calibration process.

The flowchart shown in Figure 4 summarizes all steps considered necessary in the context of the proposed calibration strategy. The parameter $W_{1,l,\exp}$ (in W/m) appearing in the input symbol of the flowchart represents the measured value of the total sheath losses due to circulating and eddy currents for the PL 1 × 300 RM 6/10 kV cables. This is the initial type of MV cables herein because it was used in the experiments conducted in [9]. Another cable shown in the flowchart is of the type Cu/XLPE/CTS/PVC/AWA/PVC 1 × 300 RMC/25 19/33 kV, which is used only in FEM-based simulations. The first type of MV cables is equipped with a metallic sheath only, therefore only the accompanying losses and loss factors ($W'_{1,l}$, $W''_{1,l}$, $W_{1,l}$, Λ'_1, Λ''_1 and Λ_1) can be calculated in Calibration Step 1. However, the second type of MV cables contains a metallic screen and a metallic armor; thus, in addition to losses and loss factors for the screen ($W'_{1,l}$, $W''_{1,l}$, $W_{1,l}$, Λ'_1, Λ''_1 and Λ_1), losses and loss factors for the armor ($W'_{2,l}$, $W''_{2,l}$, $W_{2,l}$, Λ'_2, Λ''_2 and Λ_2) must also be calculated. All these losses and loss factors appear in the output symbol of the flowchart. In the decision symbol of the flowchart, there is a condition that the percentage difference between the calculated and measured values of the total sheath/screen losses should be less than or equal to 5%. This condition was chosen empirically, that is, based on comparisons of simulated and experimental data reported by many other researchers.

B. EXPERIMENTAL VALIDATION AND SIMULATION-BASED VERIFICATION

Table 2 shows cable insulation types and service conditions used in the seven calibration steps. In each of the calibration steps where changes in the maximum temperatures of conductors, screens/sheaths and armors occurred, the values of the corresponding maximum AC resistances were recalculated in order to take into account the effect of temperature (in addition to the skin and proximity effects). In this regard, the changes in the maximum AC resistance R_C are shown in the last column of Table 2.

For the phase currents of 100 A (in Calibration Steps 1-5), the values of the maximum AC resistance R_C are calculated assuming a conductor temperature of 25 °C. It is also assumed that the phase currents applied in the experiments from [9] were almost four times lower than the corresponding ampacity, which is 378.17 A for the case of Calibration Step 1. This ampacity was calculated using the IEC-based model from Section III-A for $\theta_{C,cp} = 70°\text{C}$, $R_C = 68.266\ \mu\Omega/\text{m}$, $W_{d,l} = 0.074197$ W/m and the design where sheaths are bonded and earthed at both ends. These two assumptions are based on the fact that the experiments for the purposes of research [9] were performed quickly, probably within a few seconds, in order to avoid the effects of temperature on circulating- and eddy-current losses in lead sheaths of the three PL 1 × 300 RM 6/10 kV cables. Furthermore, Calibration Steps 6 and 7 deal with the conductor AC resistance R_C which is taken from [4] and which corresponds to the continuously permissible temperature of XLPE-insulated cables $\theta_{C,cp} = 90°\text{C}$.

Figure 5 shows distributions of temperature and magnetic field strength over the part of First Computational Domain in Figure 1a containing the PL 1 × 300 RM 6/10 kV cables, while Figure 6 shows distributions of conduction current density over the same domain. Figures 5a, 5b and 6a refer to the first sheath bonding design, while Figure 6b refers to the second one. All the distributions were generated in Calibration Step 1.

According to Figure 5a, the maximum conductor temperature and the specific temperatures of isotherms around and within the cables are not significantly higher than the ambient temperature at which the experiment was performed in [9]. In addition, according to Figure 5b, the isomagnetic contours are regular in shape and concentric with respect to the axis of trefoil non-touching formation. This indicates a negligible influence of the earth surface (which separates the native soil and the air) on the distribution of magnetic field strength over the computational domain.

Furthermore, the minimum values of conduction current densities from Figures 6a and 6b indicate that there are losses in the cable sheaths due to circulating and eddy currents. Specifically, the sheaths in Figure 6a are heated by circulating and eddy currents, while the sheaths in Figure 6b are heated only by eddy currents. The result in Figure 6a corresponds to the experiment from [9], while the result in Figure 6b has no experimental background. The current density distribution from Figure 6b was generated for the purposes of identifying and quantifying losses due to eddy currents in the given case. Based on Figure 6a, the total sheath losses due to circulating and eddy currents $W_{1,l}$ are 0.47339 W/m, which is 2.688 % higher than the corresponding value measured in [9], i.e., $W_{1,l,\text{exp}} = 0.461$ W/m. All these indicate that the basic calibration model was properly created and experimentally validated.

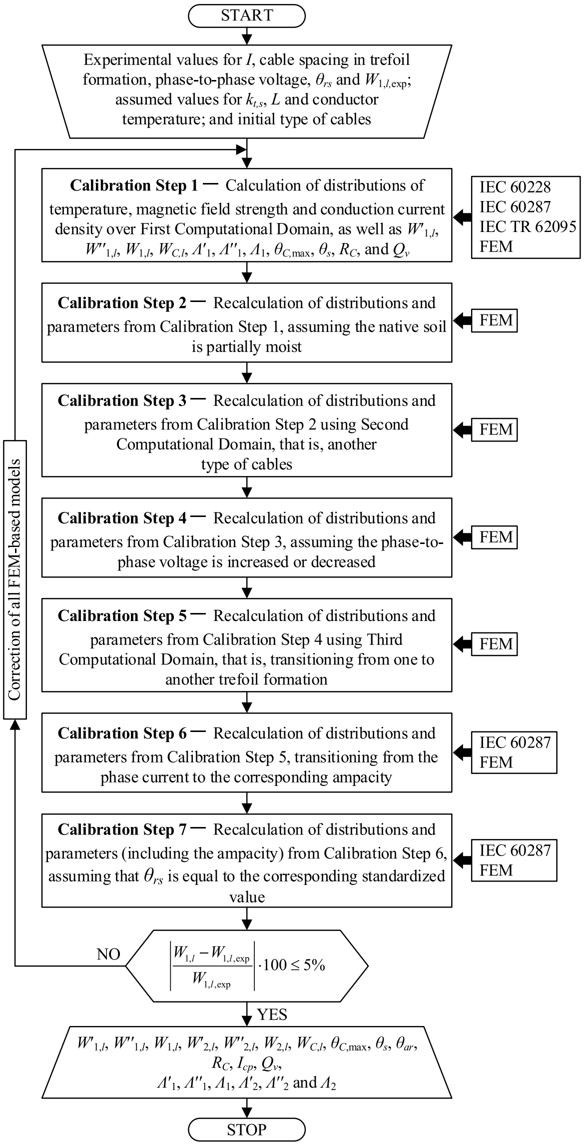

FIGURE 4. Flowchart of the proposed calibration strategy.

TABLE 2. Insulation types and service conditions appearing in steps of the calibration.

Calibr. step	Insulation type	I or I_{cp} A	Voltage kV	Spacing m	$k_{t,s}$ W/(K·m)	θ_{rs} °C	R_C μΩ/m
1	MI paper	100	10	0.098	0.4	20	58.531
2	MI paper	100	10	0.098	**0.833** [a]	20	58.531
3	**XLPE** [a]	100	10	0.098	0.833	20	**62.834** [a]
4	XLPE	100	**33** [a]	0.098	0.833	20	62.834
5	XLPE	100	33	**0.0545** [a]	0.833	20	**63.364** [a]
6	XLPE	**516.558** [a]	33	0.0545	0.833	20	**78.3** [a]
7	XLPE	**534.713** [a]	33	0.0545	0.833	**15** [a]	78.3

[a] The parameters in bold indicate a change in their type or value compared to the previous calibration step.

For Calibration Step 1, that is, for the basic calibration model, the sheath circulating- and eddy-current losses, total sheath losses and conductor losses are listed in the first row of Table 3. In addition, the accompanying loss factors are listed in the first row of Table 4. The losses were obtained by a combination of the relevant IEC formulas and FEM, while the loss factors were obtained by applying FEM only. These parameters were also determined for Calibration Step 2 and provided in the same tables. In Calibration Step 3, the calibration strategy switched from the PL 1 × 300 RM 6/10 kV cables to the Cu/XLPE/CTS/PVC/AWA/PVC 1 × 300 RMC/25 19/33 kV cables, so instead of sheath losses, appropriate screen, armor and conductor losses appear in the third row of Table 3. The accompanying screen and armor loss factors are provided in the third row of Table 4. The remaining rows of Tables 3 and 4 contain screen, armor and conductor losses, as well as the corresponding loss factors, which were generated in Calibration Steps 4–7.

Compared to the basic calibration model, in Calibration Step 2, the thermal conductivity of the native soil was approximately doubled in order to show how replacing the surrounding medium would affect the maximum sheath temperature and associated loss factors. According to Tables 3 and 4, the maximum sheath temperature decreased by 1.677 °C, while the loss factors increased negligibly. Therefore, the identification of the medium that surrounded the 10 kV cables in the experiment from [9] is irrelevant for this study.

In Calibration Step 3, the PL 1 × 300 RM 6/10 cables (with 300 mm^2 round stranded copper conductors and lead sheaths) were replaced with the 33 kV cables (with 300 mm^2 round compacted stranded copper conductors, copper tape screens and aluminum wire armors), assuming that their rated phase-to-phase voltages are 10 kV. According to Table 2, in this step, there are changes in the conductor AC resistance and the type of insulation, as well as the thermal conductivity of the insulation. These changes, according to Tables 3 and 4, led to a logical redistribution of losses across the metallic cable construction elements and to a minor increase in the maximum screen temperature of 0.644 °C. From this step onwards, the maximum armor temperature appears and is approximately equal to the maximum screen temperature.

The change from a phase-to-phase voltage of 10 kV to 33 kV in Calibration Step 4 did not lead to any significant change in temperatures, resistances, losses or loss factors (Tables 2, 3 and 4). This can be justified by the fact that dielectric losses are negligible for both voltages according to IEC 60287-1-1 [3]. Reducing the axial spacing between cables in Calibration Step 5 brought all heat sources closer together. However, this led to a decrease in the maximum conductor temperature from 22.761 °C to 22.582 °C, and an increase in the conductor AC resistance from 62.834 $\mu\Omega$/m to 63.364 $\mu\Omega$/m (Table 2). According to Table 3, this also led to minor reductions in the maximum temperatures of the screens and armors, as well as to an increase in conductor losses and certain reductions in total screen and armor losses. The resulting redistribution of losses in this step is solely due to the skin and proximity effects, and the screen/sheath, hence armor loss factors from Table 4 are expected, logical and valid.

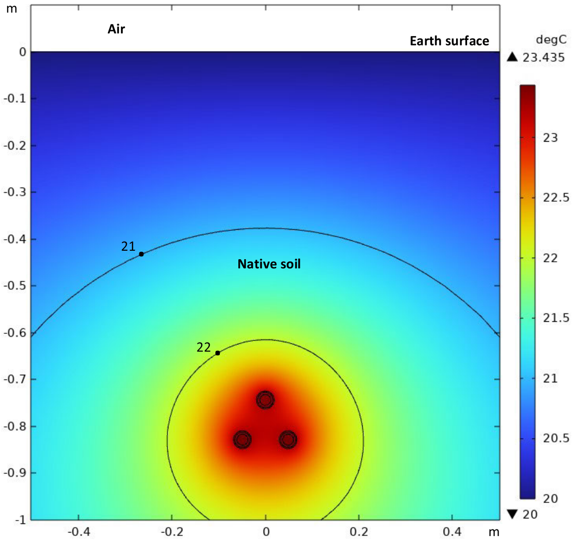

(a) Temperature distribution

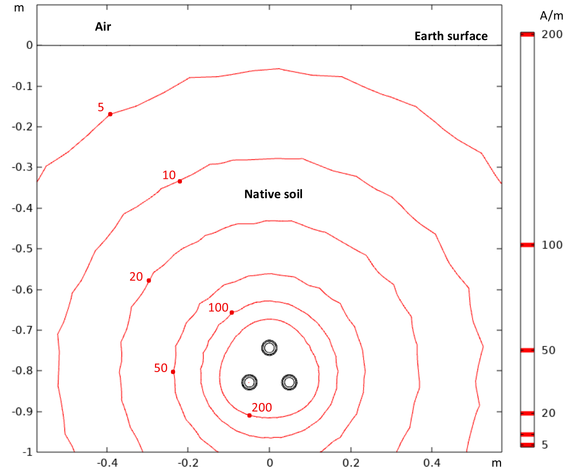

(b) Distribution of the magnetic field strength

FIGURE 5. The distributions of temperature and magnetic field strength over the part of First Computational Domain in Figure 1a that contains the PL 1 × 300 RM 6/10 kV cables, obtained in Calibration Step 1 for the design where sheaths are bonded and earthed at both ends. Contours with associated numbers indicate isotherms in (a), and isomagnetic contours in (b).

Increasing the phase currents from 100 A to the ampacity of 516.558 A, according to Tables 2, 3 and 4, resulted in significant increases in the conductor AC resistances, temperatures of all cable construction elements and all losses, but not in the corresponding loss factors. The ampacity represents an IEC-based value and was calculated according to Section III-A at an ambient temperature of 20 °C. The corresponding maximum conductor temperature is 88.699 °C. The increases are expected, while, in relation to the corresponding losses from Calibration Step 5, the reductions in the loss factors are a consequence of various multiple increases of losses in conductors (32.97 times), screens (24.27 times) and armors (24.39 times). Accordingly, Calibration Step 6 provided a reliable solution as well.

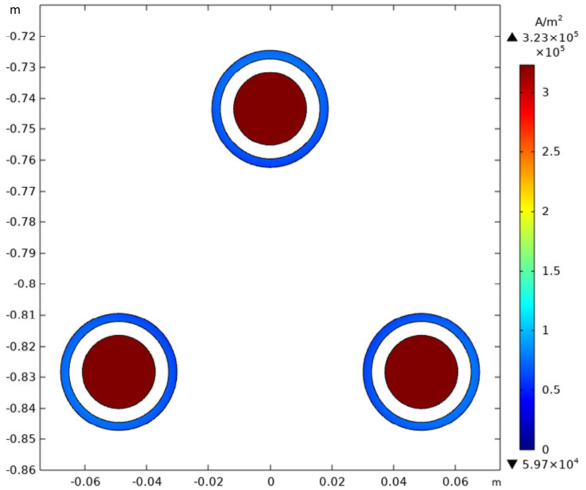

(a) Sheaths bonded and earthed at both ends

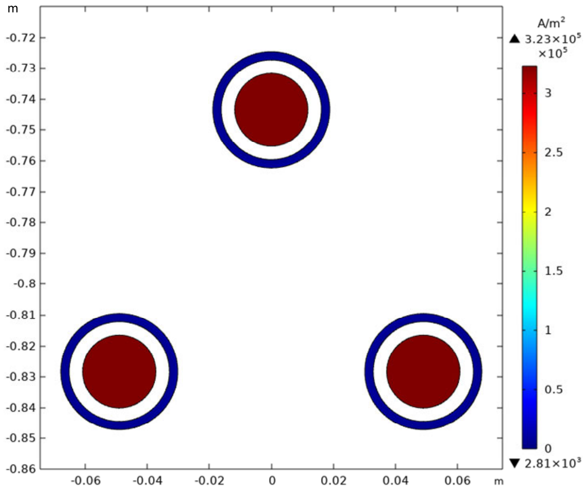

(b) Sheaths bonded and earthed at one end

FIGURE 6. **The distributions of conduction current density over the part of First Computational Domain in Figure 1a that contains the PL 1 × 300 RM 6/10 kV cables, obtained in Calibration Step 1 for the designs where sheaths are bonded and earthed at both ends and at one end, respectively.**

TABLE 3. **Screen/sheath, armor and conductor losses calculated using FEM or analytically based on the obtained numerical results.**

Calibr. step	$3W_{1,l}$ / $3W_{2,l}$ [a] W/m	θ_s / θ_{ar} [a] °C	F_s / F_{ar} [c] –	$3W''_{1,l}$ at θ_s / $3W''_{2,l}$ at θ_{ar} [b] W/m	$3W'_{1,l}$ / $3W'_{2,l}$ [d] W/m	$3W_{C,l}$ [a] W/m
Screen or sheath losses $W'_{1,l}$, $W''_{1,l}$, and $W_{1,l}$						
1	0.47339	23.233	0.978619	0.00426	0.46923	1.756
2	0.47641	21.556	0.984008	0.00428	0.47220	1.756
3	0.21829	22.200	0.993352	0.00521	0.21311	1.885
4	0.21827	22.482	0.995599	0.00521	0.21309	1.885
5	0.12169	22.307	0.993358	0.01761	0.10420	1.901
6	2.95330	80.419	0.995614	0.39417	2.56086	62.686
7	3.16730	79.728	0.995598	0.42312	2.74604	67.162
Armor losses $W'_{2,l}$, $W''_{2,l}$, and $W_{2,l}$						
1	–	–	–	–	–	1.756
2	–	–	–	–	–	1.756
3	1.1638	22.150	0.796075	0.04308	1.12951	1.885
4	1.1638	22.422	0.796427	0.04304	1.12952	1.885
5	0.6201	22.249	0.796203	0.14591	0.50390	1.901
6	15.125	78.885	0.855833	3.26080	12.3343	62.686
7	16.229	78.085	0.855291	3.50120	13.2345	67.162

[a] Parameters calculated using the FEM in COMSOL for the design where screens and armors (or sheaths only) are bonded and earthed at both ends.

[b] Parameters calculated using the FEM in COMSOL for the design where screens and armors (or sheaths only) are bonded and earthed at one end, and the maximum temperature of the screen (or sheath) θ_s or armor θ_{ar} adjusted gradually by increasing the ambient temperature θ_{rs}.

[c] Parameters calculated analytically using Equation (8) for the reactance X that takes into account changes in the axial spacing between cables.

[d] Parameters calculated analytically using the following formula:
$3W'_{1,l}=3(W_{1,l}-F_sW''_{1,l})$ – for screen/sheath losses due to circulating currents,
or $3W'_{2,l}=3(W_{2,l}-F_{ar}W''_{2,l})$ – for armor losses due to circulating currents.

TABLE 4. **Screen/sheath and armor loss factors calculated based on screen/sheath, armor and conductor losses from Table 3.**

Calibr. step	Λ'_1 –	Λ''_1 –	Λ_1 –	Λ'_2 –	Λ''_2 –	Λ_2 –
1	0.26723	0.00242	0.26960	–	–	–
2	0.26892	0.00244	0.27132	–	–	–
3	0.11306	0.00276	0.11580	0.59921	0.02285	0.61740
4	0.11304	0.00276	0.11579	0.59922	0.02283	0.61740
5	0.05482	0.00926	0.06402	0.26508	0.07676	0.32620
6	0.04085	0.00629	0.04711	0.19676	0.05202	0.24128
7	0.04089	0.00630	0.04716	0.19705	0.05213	0.24164

Finally, in Calibration Step 7, the ambient temperature was reduced from 20 °C to 15 °C and, at the same time, the cable ampacity was increased from 516.558 A to 534.713 A (by 3.514 %). Again the ampacity is an IEC-based value calculated according to Section III-A. In COMSOL, this ampacity provided a maximum conductor temperature of 88.597 °C. In addition, the conductor AC resistance remained the same, all losses increased by a certain percentage, and all loss factors remained approximately the same as in Calibration Step 6. This result also indicates that the created FEM-based model with the BS 6622 cables is highly reliable in terms of electromagnetic phenomena and heat transfer processes.

After switching from the computational domain in Figure 1a (First Computational Domain) to that in Figure 2a (Third Computational Domain), it is interesting to see what happens to the shapes of isotherms and isomagnetic contours, as well as to distributions of conduction current density for both screen bonding designs. Distributions of temperature and magnetic field strength over the part of Third Computational Domain with the Cu/XLPE/CTS/PVC/AWA/PVC 1 × 300 RMC/25 19/33 kV cables are shown in Figures 7a and 7b, respectively. Additionally, the distributions of conduction current density over the same domain part for the designs where screens and armors are bonded and earthed at both ends and at one end are shown in Figures 8a and 8b, respectively. All the distributions from Figures 7 and 8 correspond to Calibration Step 7.

As in Figures 5a and 5b, the isotherms and isomagnetic contours from Figures 7a and 7b are concentric with respect to the axis of the trefoil touching formation and their shapes remained regular (approximately elliptic or circular). The effect of the earth surface on the isomagnetic contours is again absent or negligible. As for the isotherms, it can be noted that their shapes are satisfactory in terms of axial aligning downwards relative to the earth surface, which means that the effect of the earth surface is small. This is consistent with the observations from [30].

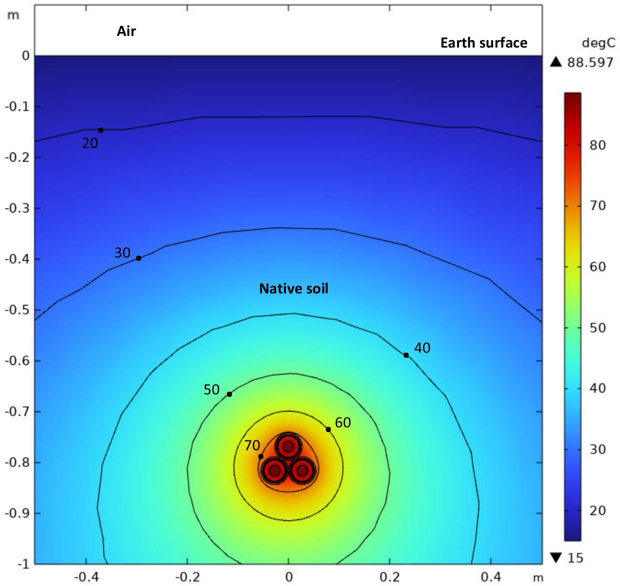

(a) Temperature distribution

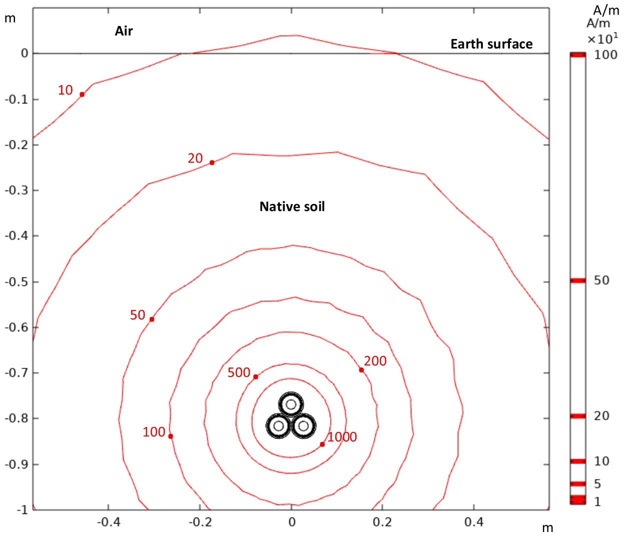

(b) Distribution of the magnetic field strength

FIGURE 7. The distributions of temperature and magnetic field strength over the part of Third Computational Domain in Figure 2a that contains the Cu/XLPE/CTS/PVC/AWA/PVC 1 × 300 RMC/25 19/33 kV cables, obtained in Calibration Step 7 for the design where screens and armors are bonded and earthed at both ends. Contours with associated numbers indicate isotherms in (a), and isomagnetic contours in (b).

Figure 8a shows the existence of a non-uniform distribution of current density over the cross-sections of individual aluminum wires in the armors, as well as that the wires closest to the axis of the trefoil formation have the lowest current density. The same applies to the aluminum wire armors in Figure 8b, except that here the conduction current densities are significantly lower. The most important detail in Figure 8b is the existence of eddy currents in the aluminum wire armors, the effects of which are ignored by default in the relevant IEC-based ampacity calculations.

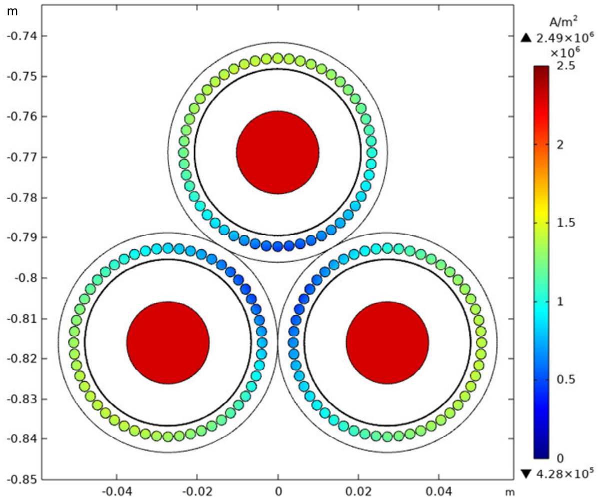

(a) Screens and armors bonded and earthed at both ends

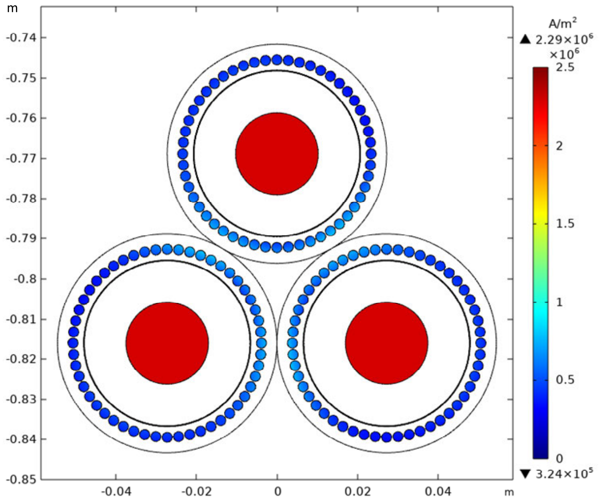

(b) Screens and armors bonded and earthed at one end

FIGURE 8. The distributions of conduction current density over the part of Third Computational Domain in Figure 2a that contains the Cu/XLPE/CTS/PVC/AWA/PVC 1 × 300 RMC/25 19/33 kV cables, obtained in Calibration Step 7 for the designs where screens and armors are bonded and earthed at both ends and at one end, respectively.

C. FINITE ELEMENT MESH INDEPENDENCE TESTS

A series of FE mesh independence (or convergence) tests were performed to verify the accuracy of the FEM-based models used in the calibration strategy. Specifically, FE mesh independence tests were performed for First, Second and Third Computational Domains, that is, for Calibration Steps 1, 3 and 7. The model used in Calibration Steps 6 and 7 represents the reference FEM-based model. In these tests, the change in the maximum conductor temperature $\theta_{C,\max}$ was monitored depending on the numbers of finite elements and nodes in meshes generated within the computational domains used. The numbers of elements and nodes were varied from those associated with automatic mesh generation to the numbers of elements and nodes associated with the first and second mesh refinements. The results of these FE mesh independence tests are listed in Table 5.

TABLE 5. Results of FE mesh independence tests for some of the used computational domains.

Comput. domain	Calibr. step	Number of nodes in FE mesh	Number of elements in FE mesh	$\theta_{C,\max}$ °C	Temperature difference °C
Automatically generated FE mesh					
First	1	2430	4796	23.434596	–
Second	3	24422	48780	22.457044	–
Third	7	23448	46832	88.597430	–
FE mesh after the first refinement					
First	1	2552	5024	23.434525	-0.000071
Second	3	24570	49060	22.457024	-0.000020
Third	7	23555	47030	88.596655	-0.093382
FE mesh after the second refinement					
First	1	3270	6428	23.434811	0.000215
Second	3	27899	55686	22.457190	0.000146
Third	7	26750	53388	88.601310	-0.089779

The differences between the maximum conductor temperatures generated using different FE meshes were lower than 0.095 °C for First, Second and Third Computational Domains. In particular, it is found that the variations in the maximum conductor temperatures of the PL 1 × 300 RM 6/10 and Cu/XLPE/CTS/PVC/AWA/PVC 1 × 300 RMC/25 19/33 kV cables do not affect their ampacities to a considerable extent. This suggests that the accuracy of one reference and 11 additional FEM-based models from the numbers of finite elements and nodes will be ensured using the automatically generated FE meshes.

V. RESULTS AND DISCUSSION

This section presents the results of the simulations performed with Third Computational Domain and 11 additional computational domains, that is, the domain in Figure 2a and each of the 12 considered Cu/XLPE/CTS/PVC/AWA/PVC 1/C 19/33 kV cables individually in that domain. For the cables with conductor cross-sections ranging from 70 to 630 mm^2, it is assumed that screens and armors are bonded and earthed at both ends. At the same time, for cables with conductor cross-sections of 800 and 1000 mm^2, screens and armors are assumed to be bonded and earthed at one end only – as it is the case in practice. Each of the simulations was performed with the ampacity calculated analytically according to Section III-A, as well as based on Calibration Step 7 from Section IV. Finally, the ampacities were recalculated in COMSOL to correspond exactly to the continuously permissible temperature of 90 °C.

Table 6 outlines the conductor AC resistances, ampacities and conductor losses taken into account or calculated analytically according to Section III-A. In particular, the values of conductor AC resistance are taken from [4]. This table also outlines the maximum temperatures of conductors, screens and armors calculated using the FEM according to Sections III-B and III-C. The parameters are provided for 12 cables of the type Cu/XLPE/CTS/PVC/AWA/PVC 1/C 19/33 kV and one of the two considered screen bonding designs.

TABLE 6. Conductor AC resistances, Ampacities and conductor losses taken from literature or calculated analytically, and maximum temperatures of conductors, screens and armors calculated using FEM for 12 different cables of the type Cu/XLPE/CTS/PVC/AWA/PVC 1/C 19/33 kV.

Conductor cross-section mm^2	R_C μΩ/m	I_{cp} A	$3W_{C,l}$ W/m	$\theta_{C,\max}$ °C	θ_s °C	θ_{ar} °C
70	342	263.070	71.005	90.606	75.573	73.659
95	247	311.285	71.802	90.455	76.602	74.767
120	196	350.147	72.091	90.296	77.195	75.425
150	159	385.797	70.996	89.887	78.071	76.193
185	127	429.417	70.256	89.611	78.622	76.839
240	97.4	485.996	69.015	89.090	79.463	77.789
300	78.3	534.713	67.162	88.597	79.728	78.085
400	62.2	586.656	64.221	87.842	80.063	78.543
500	49.6	642.154	61.359	87.184	80.076	78.630
630	39.9	696.845	58.125	86.248	80.222	78.929
800 [a]	33.1	911.263	82.459	90.558	82.952	81.291
1000 [a]	28.4	978.110	81.511	90.540	83.291	81.659

[a] The rated cross-sections for which screens and armors are bonded and earthed at one end.

Based on Table 6, conductor losses first increase (for the first three cross-sections), then decrease and finally increase again. With the exception that there is no increase of the maximum conductor temperature for the first three cross-sections, the change in the maximum conductor temperature follows the change in conductor losses. A deviation in the maximum conductor temperature is observed from the corresponding continuously permissible value, which means that the analytical ampacities do not correspond to those that can be obtained using FEM. This will ultimately result in a correction of the FEM-based values for the screen and armor loss factors Λ_1 and Λ_2, as well as the ampacity I_{cp}.

Figure 9 shows the total screen losses $W_{1,l}$, the screen eddy-current losses $W''_{1,l}$, the total armor losses $W_{2,l}$ and the armor eddy-current losses $W''_{2,l}$ calculated using FEM in COMSOL for 12 different BS 6622 cables. This bar diagram also shows the screen circulating-current losses $W'_{1,l}$ calculated using Equation (2) based on the numerical values of $W_{1,l}$ and $W''_{1,l}$, as well as the armor circulating-current losses $W'_{2,l}$ calculated using Equation (3) based on the numerical values of $W_{2,l}$ and $W''_{2,l}$.

The most important detail in Figure 9 is the existence of eddy-current losses in aluminum wire armors which are higher than, or comparable to some other screen and armor losses, but are not negligible. Specifically, armor eddy-current losses increase with increasing conductor cross-section, that is, with increasing effective cross-section of aluminum wire armor. This is contrary to the recommendation of IEC 60287-1-1 [3], which states that losses due to eddy currents in non-magnetic wire armors of power cables can be ignored. Further, screen and armor losses are used for the calculation of the screen and armor loss factors Λ'_1, Λ''_1, Λ_1, Λ'_2, Λ''_2 and Λ_2 using FEM.

The screen loss factors calculated analytically according to Section III-A (λ'_1, λ''_1 and λ_1) and numerically according to Sections III-B and III-C (Λ'_1, Λ''_1 and Λ_1) are presented comparatively in Table 7.

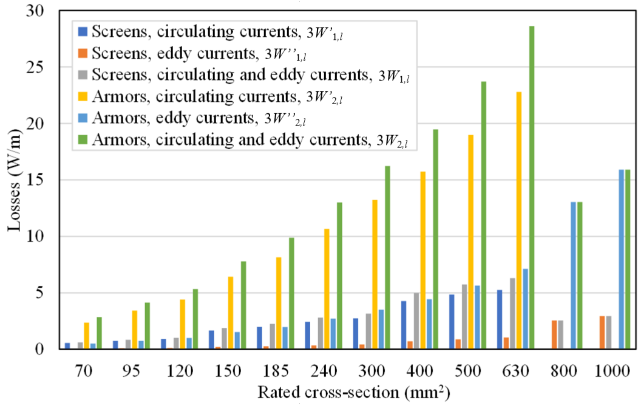

FIGURE 9. Screen and armor losses calculated using FEM or analytically based on associated FEM-based losses for 12 different cables of the type Cu/XLPE/CTS/PVC/AWA/PVC 1/C 19/33 kV. For rated cross-sections of 800 mm^2 and 1000 mm^2, screen and armor losses correspond to the design where screens and armors are bonded and earthed at one end.

TABLE 7. Screen loss factors calculated analytically and using FEM for 12 different cables of the type Cu/XLPE/CTS/PVC/AWA/PVC 1/C 19/33 kV.

Conductor cross-section mm^2	λ'_1 –	Λ'_1 –	λ''_1 –	Λ''_1 –	λ_1 –	Λ_1 –
70	0.00693	0.00796	0.00089	0.00094	0.00783	0.00890
95	0.00939	0.01060	0.00126	0.00132	0.01065	0.01191
120	0.01155	0.01267	0.00163	0.00167	0.01317	0.01434
150	0.02129	0.02353	0.00297	0.00302	0.02424	0.02654
185	0.02595	0.02857	0.00376	0.00386	0.02970	0.03241
240	0.03259	0.03549	0.00503	0.00518	0.03760	0.04065
300	0.03927	0.04089	0.00635	0.00630	0.04559	0.04716
400	0.06543	0.06670	0.01137	0.01123	0.07670	0.07783
500	0.07912	0.07931	0.01467	0.01450	0.09366	0.09369
630	0.09417	0.09078	0.01868	0.01812	0.11270	0.10875
800 [a]	0	0	0.03264	0.03097	0.03264	0.03097
1000 [a]	0	0	0.03873	0.03625	0.03873	0.03626

[a] The rated cross-sections for which screens and armors are bonded and earthed at one end.

Table 9 summarizes the results on comparing the values of the screen and armor loss factors calculated using FEM in COMSOL (according to Sections III-B and III-C) with those obtained analytically (according to Section III-A). Specifically, Table 9 shows the differences between the numerical values of the screen and armor loss factors and their corresponding analytical values.

According to Table 9, the largest differences are found in the armor circulating-current loss factor, while the smallest differences are found in the armor eddy-current loss factor. The deviations of the armor circulating-current loss factors obtained using FEM from those obtained analytically lie in the range of -15.741% to -20.775%. In addition, the deviations of the armor eddy-current loss factors obtained numerically from those obtained analytically are between –2.22% and 0.765%. Moreover, for the screen circulating-current loss factor, these differences are between -3.606% and 14.768%. Furthermore, the differences between the analytical and numerical values of the screen eddy-current loss factor lie in the range of -6.398% to 5.302%, and so on.

TABLE 8. Armor loss factors calculated analytically and using FEM for 12 different cables of the type Cu/XLPE/CTS/PVC/AWA/PVC 1/C 19/33 kV.

Conductor cross-section mm^2	λ'_2 –	Λ'_2 –	λ''_2 –	Λ''_2 –	λ_2 –	Λ_2 –
70	0.03967	0.03325	0.00714	0.00719	0.04638	0.04001
95	0.05694	0.04788	0.01050	0.01058	0.06675	0.05775
120	0.07274	0.06129	0.01387	0.01397	0.08564	0.07428
150	0.11134	0.09068	0.02140	0.02154	0.13028	0.10975
185	0.14229	0.11596	0.02799	0.02817	0.16685	0.14069
240	0.19001	0.15444	0.03908	0.03935	0.22390	0.18855
300	0.24292	0.19705	0.05173	0.05213	0.28717	0.24164
400	0.30611	0.24489	0.06891	0.06911	0.36426	0.30322
500	0.38917	0.30945	0.09189	0.09218	0.46576	0.38628
630	0.49483	0.39203	0.12214	0.12269	0.59480	0.49246
800 [a]	0	0	0.16152	0.15819	0.16152	0.15819
1000 [a]	0	0	0.19953	0.19510	0.19953	0.19510

[a] The rated cross-sections for which screens and armors are bonded and earthed at one end.

TABLE 9. Differences between analytical and numerical values of the screen and armor loss factors calculated for 12 different cables of the type Cu/XLPE/CTS/PVC/AWA/PVC 1/C 19/33 kV.

Conductor cross-section mm^2	Diff. btw. λ'_1 & Λ'_1 %	Diff. btw. λ''_1 & Λ''_1 %	Diff. btw. λ_1 & Λ_1 %	Diff. btw. λ'_2 & Λ'_2 %	Diff. btw. λ''_2 & Λ''_2 %	Diff. btw. λ_2 & Λ_2 %
70	14.768	5.302	13.688	-16.192	0.696	-13.749
95	12.826	4.697	11.864	-15.923	0.676	-13.485
120	9.752	2.769	8.892	-15.741	0.702	-13.264
150	10.533	1.811	9.470	-18.550	0.656	-15.757
185	10.091	2.607	9.147	-18.503	0.642	-15.684
240	8.913	2.928	8.116	-18.722	0.686	-15.785
300	4.118	-0.812	3.434	-18.883	0.765	-15.855
400	1.941	-1.172	1.484	-19.998	0.290	-16.759
500	0.243	-1.149	0.027	-20.485	0.325	-17.063
630	-3.606	-2.995	-3.506	-20.775	0.457	-17.207
800 [a]	–	-5.112	-5.112	–	-2.062	-2.062
1000 [a]	–	-6.398	-6.382	–	-2.220	-2.220

[a] The rated cross-sections for which screens and armors are bonded and earthed at one end.

Table 10 shows the total screen and armor loss factors together with the ampacities recalculated using FEM in COMSOL to correspond exactly with the continuously permissible temperature of 90 °C. The first column of Table 10 provides the rated cross-sections of conductors and screens for 12 cables of the type Cu/XLPE/CTS/PVC/AWA/PVC 1/C 19/33 kV, while the second column of the table provides the data on the accompanying armors. This table also shows the ampacities calculated according to IEC 60287-1-1 [3] and already provided in [4].

Compared to the corresponding values in Tables 7 and 8, the total screen and armor loss factors listed in Table 10 differ only slightly. However, the differences between the ampacities obtained using FEM and the ones taken from [4] range from 0.316 A – for a 70 mm^2 conductor and –0.166 A

TABLE 10. **Ampacities calculated analytically and using FEM for 12 different cables of the type Cu/XLPE/CTS/PVC/AWA/PVC 1/C 19/33 kV.**

Conductor/ screen cross-section [a] mm^2/mm^2	Armor [a] No. of wires/ Wire diameter –/mm	I_{cp} [b] taken from Ref. [4] A	Parameters obtained using FEM in COMSOL for $\theta_{C,cp}$=90 °C		
			Λ_1 –	Λ_2 –	I_{cp} A
70/16	48/2	262.321	0.00891	0.04005	262.005
95/16	51/2	310.168	0.01193	0.05780	310.334
120/16	53/2	348.664	0.01435	0.07432	349.448
150/25	44/2.5	384.343	0.02654	0.10973	386.093
185/25	46/2.5	427.668	0.03239	0.14060	430.555
240/25	49/2.5	484.349	0.04059	0.18829	489.038
300/25	52/2.5	533.130	0.04706	0.24115	539.915
400/35	55/2.5	587.154	0.07761	0.30239	595.530
500/35	58/2.5	643.392	0.09336	0.38500	654.950
630/35	62/2.5	700.680	0.10829	0.49047	715.575
800/50	68/2.5	879.755 [c]	0.03101 [c]	0.15839 [c]	907.790 [c]
1000/50	72/2.5	939.099 [c]	0.03630 [c]	0.19533 [c]	974.485 [c]

[a] The rated cross-sections of conductors and screens in the first column, and numbers and diameters of wires in armors in the second column.

[b] The ampacities calculated analytically in Reference [4] for $\theta_{C,cp}$=90 °C.

[c] The parameters corresponding to the design where screens and armors are bonded and earthed at one end.

– for a 95 mm^2 conductor to –14.895 A – for a 630 mm^2 conductor and –35.386 A – for a 1000 mm^2 conductor. If the numerical ampacities from Table 10 are now compared with the analytical ones from Table 6, the differences are found in the range from –18.73 A – for a 630 mm^2 conductor to 3.625 A – for a 1000 mm^2 conductor.

It is important to recall here that the ampacities from the third column of Table 10 do not take into account the effect of armor eddy-current losses (i.e., $\lambda_2'' = 0$). Conversely, the ampacities from Table 6 take this effect into account. Having this in mind, for both screen bonding designs, the differences between the IEC-based ampacities from Table 6 and the FEM-based ampacities from the last column of Table 10 are smaller in 7 out of 12 cases.

VI. CONCLUSION

This paper demonstrated that eddy-current losses occur in non-magnetic wire armors of three BS 6622 single-core cables installed directly in the soil in both trefoil non-touching and trefoil touching formations. For both considered screen bonding designs, these losses cannot be neglected in either IEC- or FEM-based ampacity calculations.

For conductor cross-sections ranging from 70 to 1000 mm^2, the FEM-based screen and armor eddy-current loss factors lie within the ranges of 0.00094–0.03625 and 0.00719–0.1951, respectively. The corresponding deviations between the FEM- and IEC-based loss factors are between -6.398% and 5.302%.

The quantitative separation of individual screen and armor eddy-current losses clearly indicates that the existing IEC-based ampacity calculation procedures should be adequately amended and harmonized with the recommendations provided in the technical brochures CIGRÉ TB 272 and CIGRÉ TB 880.

For three PL 1 × 300 RM 6/10 kV cables installed in trefoil non-touching formation, the total sheath losses due to circulating- and eddy-currents obtained using FEM are 2.688% higher than the corresponding measured losses, confirming very good agreement between numerical and experimental results.

The proposed new hybrid FEM-based procedure for the quantitative separation of eddy-current losses from circulating-current losses and for the calculation of cable ampacities was experimentally validated. It was also shown that the procedure is accurate, equivalent to the existing experimentally based approaches, and applicable to a wide range of power cable types.

In addition, the new calibration strategy employed in this study constitutes an independent contribution, providing a reliable FEM-based electro–magneto–thermal reference model for cable ampacity calculations.

For both screen bonding designs, the differences between IEC- and FEM-based cable ampacities are generally smaller when IEC-based calculations explicitly account for armor eddy-current losses.

Future work will focus on extending the proposed methodology to BS 6622 cables installed directly in the soil in flat non-touching and touching formations. Further developments may include FEM-based electro–magneto–thermal models in which non-magnetic wire armors are represented by equivalent cylindrical layers with identical effective cross-sections, as well as potential amendments to the existing IEC recommendations for calculating screen and armor eddy-current loss factors.

REFERENCES

[1] K. Kawasaki, M. Inami, and T. Ishikawa, "Theoretical considerations on eddy current losses in non-magnetic and magnetic pipes for power transmission systems," *IEEE Trans. Power App. Syst.*, vol. PAS-100, no. 2, pp. 474–484, Feb. 1981, doi: 10.1109/TPAS.1981.316904.

[2] R. L. Jackson, "Eddy-current losses in unbonded tubes," *Proc. Inst. Electr. Eng.*, vol. 122, no. 5, pp. 551–557, May 1975, doi: 10.1049/piee.1975.0151.

[3] *Calculation of the Current Rating—Part 1–1: Current Rating Equations (100% Load Factor) and Calculation of Losses—General*, Standard 60287-1-1:2023, Jun. 2023.

[4] M. Sucurovic, D. Klimenta, and D. Tasic, "Correction of the IEC formula for the eddy-current loss factor: The case of single-core cables in trefoil formation with metallic screens bonded and earthed at one end," *Facta Universitatis-Ser., Electron. Energetics*, vol. 37, no. 2, pp. 391–408, Jun. 2024, doi: 10.2298/fuee2402391s.

[5] *Large Cross-Sections and Composite Screens Design*, CIGRÉ, Paris, France, Jun. 2005.

[6] *Power Cable Rating Examples for Calculation Tool Verification*, CIGRÉ, Paris, France, Sep. 2022.

[7] E. Kuffel and J. Poltz, "AC losses in crossbonded and bonded at both ends high voltage cables," *IEEE Trans. Power App. Syst.*, vol. PAS-100, no. 1, pp. 369–374, Jan. 1981, doi: 10.1109/TPAS.1981.316865.

[8] P. Graneau, *Underground Power Transmission*. Hoboken, NJ, USA: Wiley, 1979, pp. 58–79.

[9] A. H. M. Arnold, "The theory of sheath losses in single-conductor lead-covered cables," *J. Inst. Electr. Eng.*, vol. 67, no. 384, pp. 69–89, Dec. 1928, doi: 10.1049/jiee-1.1928.0194.

[10] R. A. Brockbank and J. K. Webb, "Sheath and armour losses in single-core cables for single-phase and three-phase transmission," *J. Inst. Electr. Eng.*, vol. 67, no. 387, pp. 337–358, Mar. 1929, doi: 10.1049/jiee-1.1929.0031.

[11] D. Labridis and P. Dokopoulos, ''Finite element computation of field, losses and forces in a three-phase gas cable with nonsymmetrical conductor arrangement,'' *IEEE Trans. Power Del.*, vol. PD-3, no. 4, pp. 1326–1333, Oct. 1988, doi: 10.1109/61.193927.

[12] D. Chatzipetros and J. A. Pilgrim, ''Impact of proximity effects on sheath losses in trefoil cable arrangements,'' *IEEE Trans. Power Del.*, vol. 35, no. 2, pp. 455–463, Apr. 2020, doi: 10.1109/TPWRD.2019.2896490.

[13] N. Kovac, I. Sarajcev, and D. Poljak, ''Nonlinear-coupled electric-thermal modeling of underground cable systems,'' *IEEE Trans. Power Del.*, vol. 21, no. 1, pp. 4–14, Jan. 2006, doi: 10.1109/TPWRD.2005.852272.

[14] J. S. Barrett and G. J. Anders, ''Circulating current and hysteresis lossesin screens,sheaths and armour of electric power cables—Mathematicalmodels and comparison with IEC standard 287,'' *IEE Proc.-Sci., Meas. Technol.*, vol. 144, no. 3, pp. 101–110, May 1997, doi: 10.1049/ip-smt:19971162.

[15] P. Zamani, A. Foomezhi, and S. G. Nohooji, ''A review of medium voltage single-core cable armouring, induced currents and losses,'' *Energy Power Eng.*, vol. 13, no. 7, pp. 272–292, Jul. 2021, doi: 10.4236/epe.2021.137019.

[16] M. Rasoulpoor, M. Mirzaie, and S. M. Mirimani, ''Electrical and thermal analysis of single conductor power cable considering the lead sheath effect based on finite element method,'' *Iran. J. Electr. Electron. Eng.*, pp. 73–81, Mar. 2016.

[17] J. J. Bremnes, G. Evenset, and R. Stølan, ''Power loss and inductance of steel armoured multi-core cables: Comparison of IEC values with 2.5D FEA results and measurements,'' in *Proc. CIGRÉ*, 2010, pp. 1–10.

[18] J. M. Lee, D. J. Park, G. Y. Jeong, T. H. Lee, J. N. Kim, S. I. Jeon, H. D. Park, and J. Kaumanns, ''Measurements and FEA results of steel armour losses in three-core submarine XLPE cables,'' *Proc. CIGRÉ*, 2016, pp. 1–7.

[19] E. Bompou, N. Mijatovic, C. Træholt, D. W. A. Willén, and C. Thidemann, ''Loss in steel armour wires for submarine power cables,'' in *Proc. IEEE Power Energy Soc. Gen. Meeting (PESGM)*, OR, USA, Germany, Aug. 2018, pp. 1–5, doi: 10.1109/PESGM.2018.8586209.

[20] J. C. del-Pino-López and P. Cruz-Romero, ''Use of 3D-FEM tools to improve loss allocation in three-core armored cables,'' *Energies*, vol. 14, no. 9, p. 2434, Apr. 2021, doi: 10.3390/en14092434.

[21] H. Strand, E. Eberg, and G. J. Anders, ''Hybrid method for numerical implementation of segmented power cable conductors in finite-element based ampacity calculation,'' in *Proc. Nordic Insul. Symp.*, Jul. 2022, vol. 27, no. 1, pp. 1–5, doi: 10.5324/nordis.v27i1.4709.

[22] T. Szczegielniak, P. Jabłoński, and D. Kusiak, ''Analytical approach to current rating of three-phase power cable with round conductors,'' *Energies*, vol. 16, no. 4, p. 1821, Feb. 2023, doi: 10.3390/en16041821.

[23] E. Lunca, S. Vornicu, and A. Sălceanu, ''Numerical and analytical analysis of the low-frequency magnetic fields generated by three-phase underground power cables with solid bonding,'' *Appl. Sci.*, vol. 13, no. 10, p. 6328, May 2023, doi: 10.3390/app13106328.

[24] M. Quercio, J. C. Del Pino Lopez, S. Grasso, and A. Canova, ''Numerical and experimental analysis of thermal behaviour of high voltage power cable in unfilled ducts,'' *Sci. Rep.*, vol. 14, no. 1, Sep. 2024, Art. no. 20599, doi: 10.1038/s41598-024-71281-x.

[25] Y.-S. Kim, H. Nguyen Cong, B. H. Dinh, and H.-K. Kim, ''Effect of ambient air and ground temperatures on heat transfer in underground power cable system buried in newly developed cable bedding material,'' *Geothermics*, vol. 125, Jan. 2025, Art. no. 103151, doi: 10.1016/j.geothermics.2024.103151.

[26] *Calculation of the Current Rating—Part 2–1: Thermal Resistance—Calculation of the Thermal Resistance*, document IEC 60287-2-1:2023, 2023.

[27] *Calculation of the Current Rating—Part 3–1: Operating Conditions—Site Reference Conditions*, document IEC 60287-3-1:2017, 2017.

[28] *Calculations for Current Ratings—Finite Element Method*, document IEC TR 62095:2003, 2003.

[29] *Armoured Cables With Thermosetting Insulation for Rated Voltages From 3.8/6.6 KV To 19/33 KV—Requirements and Test Methods*, document BS 6622:2007, 2007.

[30] D. Klimenta, M. Sucurovic, and D. Tasic, ''Amendments to some IEC TR 62095 recommendations for underground single-core power cables in trefoil formation,'' *ICCK Trans. Electric Power Netw. Syst.*, vol. 1, no. 1, pp. 38–49, Oct. 2025, doi: 10.62762/tepns.2025.641725.

[31] E. Chesnokov, E. Feklistov, G. Greshnyakov, and O. Emelyanov, ''Simulation of thermal operation modes of XLPE pulse cable,'' *ICCK Trans. Electr. Power Netw. Syst.*, vol. 1, no. 1, pp. 17–25, Oct. 2025, doi: 10.62762/tepns.2025.127082.

[32] A. H. M. Arnold, ''Eddy-current losses in single-conductor paper-insulated lead-covered unarmoured cables of a single-phase system,'' *J. Inst. Electr. Eng.-II, Power Eng.*, vol. 89, no. 12, pp. 636–645, Dec. 1942, doi: 10.1049/ji-2.1942.0105.

[33] M. Klein, *Kabeltechnik: Die Theorie, Berechnung Und Herstellung Des Elektrischen Kabels*. Berlin, Germany: Springer, 1929, doi: 10.1007/978-3-642-91803-2.

[34] *Conductors of Insulated Cables*, document IEC 60228:2023, 2023.

[35] L. Heinhold, *Power Cables Their Application—Part 1*. Berlin, Germany: Siemens Aktiengesellschaft, 1990.

[36] S. Y. King and N. A. Halfter, *Underground Power Cables*, 1st ed., White Plains, NY, USA: Longman, 1982.

[37] T. S. Freitas, A. S. Guimarães, S. Roels, V. P. de Freitas, and A. Cataldo, ''Is the time-domain reflectometry (TDR) technique suitable for moisture content measurement in low-porosity building materials?'' *Sustainability*, vol. 12, no. 19, p. 7855, Sep. 2020, doi: 10.3390/su12197855.

[38] V. Y. Grytsiuk and M. A. M. Yassin, ''Numerical modeling of coupled electromagnetic and thermal processes in the zone induction heating system for metal billets,'' *Electr. Eng. Electromechanics*, no. 2, pp. 59–68, Mar. 2025, doi: 10.20998/2074-272x.2025.2.08.

[39] J. Pilgrim, D. Swaffield, P. Lewin, S. Swingler, F. Waite, and D. Payne, ''Impact of moisture migration on the current rating of high operating temperature cables,'' in *Proc. 8th Int. Conf. Insulated Power Cables (Jicable)*, 2011, pp. 222–227.

[40] O. E. Gouda, A. Z. El Dein, and G. M. Amer, ''Effect of the formation of the dry zone around underground power cables on their ratings,'' *IEEE Trans. Power Del.*, vol. 26, no. 2, pp. 972–978, Apr. 2011, doi: 10.1109/TPWRD.2010.2060369.

[41] O. E. Gouda, G. F. A. Osman, W. A. A. Salem, and S. H. Arafa, ''Load cycling of underground distribution cables including thermal soil resistivity variation with soil temperature and moisture content,'' *IET Gener., Transmiss. Distrib.*, vol. 12, no. 18, pp. 4125–4133, Sep. 2018, doi: 10.1049/iet-gtd.2018.5589.

[42] H. P. Lidén, B. Adl-Zarrabi, and J. Sundberg, ''Drying of cable backfill by vapour diffusion balanced by capillary water suction: A laboratory experiment with altered groundwater levels,'' *Case Stud. Thermal Eng.*, vol. 47, Jul. 2023, Art. no. 102941, doi: 10.1016/j.csite.2023.102941.

[43] K.-H. Cho, ''Coupled electro-magneto-thermal model for induction heating process of a moving billet,'' *Int. J. Thermal Sci.*, vol. 60, pp. 195–204, Oct. 2012, doi: 10.1016/j.ijthermalsci.2012.05.003.

[44] A. A. Shcherba, O. D. Podoltsev, N. I. Suprunovska, R. V. Bilianin, T. Y. Antonets, and I. M. Masluchenko, ''Modeling and analysis of electrothermal processes in installations for induction heat treatment of aluminum cores of power cables,'' *Electr. Eng. Electromechanics*, no. 1, pp. 51–60, Jan. 2024, doi: 10.20998/2074-272x.2024.1.07.

[45] A. B. J. Reece and T. W. Preston, *Finite Element Methods in Electrical Power Engineering*. London, U.K.: Oxford Univ. Press, 2007.

MARKO ŠUĆUROVIĆ was born in Serbia, in 1988. He received the B.Sc. and M.Sc. degrees from the Faculty of Technical Sciences, University of Kragujevac, Čačak, in 2011 and 2012, respectively. He is currently pursuing the Ph.D. degree with the Faculty of Electronic Engineering, University of Niš. He is a Teaching and Research Assistant with the Faculty of Technical Sciences, University of Kragujevac, Čačak. His main research interests include electrical power cable engineering, renewable energy sources, electric power system components, heat transfer, FEM, and FEA.

DARDAN KLIMENTA was born in Serbia, in 1975. He received the degree from the Faculty of Electrical Engineering, University of Priština, in 1998, and the M.Sc. and Ph.D. degrees from the Faculty of Electrical Engineering, University of Belgrade, in 2001 and 2007, respectively. He is currently a Full Professor with the Faculty of Technical Sciences, University of Priština in Kosovska Mitrovica. His main research interests include electrical power cable engineering, renewable energy sources, electric power system components, heat transfer, optimization methods, FEM, and FEA.

NIKOLAY HINOV (Senior Member, IEEE) received the Ph.D. and D.Sc. degrees from the Technical University of Sofia, in 1998 and 2024, respectively. He is currently a Professor with the Department of Computer Systems, Technical University of Sofia, Bulgaria. His current research interests include artificial intelligence systems, development and design of power electronic converters with application in industrial technologies, electric vehicles, decentralized generation of electricity, and energy storage.

DRAGAN TASIĆ (Senior Member, IEEE) was born in Serbia, in 1961. He received the bachelor's and M.Sc. degrees from the Faculty of Electrical Engineering, University of Belgrade, in 1986 and 1991, respectively, and the Ph.D. degree from the Faculty of Electronic Engineering, University of Niš, in 1997. He is currently a Full Professor with the Faculty of Electronic Engineering, University of Niš. His main research interests include electrical power cable engineering, renewable energy sources, electric power system modeling and analysis, heat transfer, and optimization methods.

MLADEN BANJANIN was born in Sarajevo, Yugoslavia, in 1988. He received the B.Sc. degree from the Faculty of Electrical Engineering, University of East Sarajevo, Bosnia and Herzegovina, in 2011, and the M.Sc. and Ph.D. degrees from the School of Electrical Engineering, University of Belgrade, Serbia, in 2012 and 2017, respectively. He is currently an Associate Professor with the Faculty of Electrical Engineering, University of East Sarajevo, and a Visiting Professor with the Faculty of Electrical Engineering, University of Banja Luka. His main interests include lighting protection, high voltage engineering, and power quality.

DARIUS ANDRIUKAITIS (Member, IEEE) received the M.Sc. and Ph.D. degrees in electronics engineering, in 2005 and 2009, respectively. He is currently with the Department of Electronics Engineering, Faculty of Electrical and Electronics Engineering, Kaunas University of Technology. His research interests include finding solutions for issues related to interactive electronic systems, integrated information systems, smart transportation systems, control systems, the IoT, and WSN.

• • •